LiDAR-Based Mobile Mapping System for Lane Width Estimation in Work Zones

Ayman Habib

Yun-Jou Lin

Radhika Ravi

Tamer Shamseldin

Magdy Elbahnasawy

AUTHORS

Ayman Habib, PhD
Thomas A. Page Professor of Civil Engineering
Lyles School of Civil Engineering
Purdue University
(765) 496-0173
ahabib@purdue.edu
Corresponding Author

Yun-Jou Lin
Radhika Ravi
Tamer Shamseldin
Magdy Elbahnasawy
Graduate Research Assistants
Lyles School of Civil Engineering
Purdue University

JOINT TRANSPORTATION RESEARCH PROGRAM

NOTICE

COPYRIGHT

TECHNICAL REPORT DOCUMENTATION PAGE

1. Report No. FHWA/IN/JTRP-2018/10	2. Government Accession No.	3. Recipient's Catalog No.
4. Title and Subtitle LiDAR-Based Mobile Mapping System for Lane Width Estimation in Work Zones		**5. Report Date** May 2018
		6. Performing Organization Code
7. Author(s) Ayman Habib, Yun-Jou Lin, Radhika Ravi, Tamer Shamseldin, Magdy Elbahnasawy		**8. Performing Organization Report No.** FHWA/IN/JTRP-2018/10
9. Performing Organization Name and Address Joint Transportation Research Program Hall for Discovery and Learning Research (DLR), Suite 204 207 S. Martin Jischke Drive West Lafayette, IN 47907		**10. Work Unit No.**
		11. Contract or Grant No. SPR-4126
12. Sponsoring Agency Name and Address Indiana Department of Transportation (SPR) State Office Building 100 North Senate Avenue Indianapolis, IN 46204		**13. Type of Report and Period Covered** Final Report
		14. Sponsoring Agency Code

15. Supplementary Notes

Conducted in cooperation with the U.S. Department of Transportation, Federal Highway Administration.

16. Abstract

Lane width evaluation is one of the crucial aspects in road safety inspection. Moreover, lane width is one of the most important attributes of a road digital map for many applications, such as driver assistance systems and risk assessment. Using mobile mapping systems (MMSs) equipped with laser scanners is a safe and cost-effective method for rapidly collecting detailed information about various characteristics along any transportation corridor. This report presents an approach to derive lane width estimates using point clouds acquired from a calibrated mobile mapping system. To derive point clouds with high positional accuracy, estimation of the mounting parameters relating the different laser scanners to the onboard GNSS/INS unit is the foremost and necessary step. This report proposes a multi-unit LiDAR system calibration procedure where the mounting parameters can be estimated through minimizing the normal distance between conjugate planar/linear features in overlapping point clouds derived from different drive-runs. After generating the LiDAR point cloud using the estimated mounting parameters, the road surface can be extracted with the assistance of navigation data, which in turn is used to identify lane markings. Lane markings have a high retro-reflective property that will be exhibited as high-intensity points when scanned by a laser scanner. This property can be used to distinguish lane markings from the extracted road surface in the LiDAR point cloud. Then, non-lane marking points among the extracted high-intensity points are identified and removed. Next, the lane marking centerline is derived for lane width estimation.

17. Key Words		18. Distribution Statement		
mobile mapping system, LiDAR, lane width estimation, calibration, work zones		No restrictions. This document is available through the National Technical Information Service, Springfield, VA 22161.		
19. Security Classif. (of this report) Unclassified	**20. Security Classif. (of this page)** Unclassified		**21. No. of Pages** 49	**22. Price**

Form DOT F 1700.7 (8-72)   Reproduction of completed page authorized

EXECUTIVE SUMMARY

LIDAR-BASED MOBILE MAPPING SYSTEM
FOR LANE WIDTH ESTIMATION
IN WORK ZONES

Introduction

Road digital maps that include road characteristics (e.g., lane marking, lane width, slope, curvature, clothoid, shoulder width, and shoulder barriers) are useful for driver assistance systems, road safety inspection, traffic accident reduction, and infrastructure monitoring. FHWA reported that there were an estimated 96,626 accidents in work zones during 2015, out of which 642 accidents involved at least one fatality (FHWA, n.d.). Efficient work zone monitoring and inspection is one of the critical tasks to decrease traffic accidents. Lane width evaluation is one of the crucial aspects of road safety inspection, especially in work zones where a narrow lane width can result in a reduced roadway capacity and also increase the probability of severe accidents. In the past, collecting geospatial data for building road digital maps was an expensive, time-consuming, and labor-intensive task. Moreover, manual on-site data collection can expose field crew to dangerous road traffic. Using mobile mapping systems (MMS) equipped with Light Detection and Ranging (LiDAR) units and cameras, geo-referenced point clouds and images can be collected rapidly in work zone areas without affecting traffic. Then, road characteristics can be derived from the acquired point cloud for risk assessment.

This report presents an approach to derive lane width estimates using point clouds acquired from a calibrated mobile mapping system. To derive point clouds with high positional accuracy, estimating the mounting parameters relating the different laser scanners to the onboard GNSS/INS unit is the first and most necessary step. This report proposes a multi-unit LiDAR system calibration procedure where the mounting parameters can be estimated through minimizing the normal distance between conjugate planar/linear features in overlapping point clouds derived from different drive-runs. To increase the efficiency of semi-automatic conjugate feature extraction from the LiDAR data, specifically designed calibration boards covered by highly reflective surfaces that could be easily deployed and set up within outdoor environments are used in this study. After generating the LiDAR point cloud using the estimated mounting parameters, the road surface can be extracted with the assistance of navigation data, which in turn is used to identify lane markings. Lane markings have a high retro-reflective property that will be exhibited as high intensity points when scanned by a laser scanner. This property can be used to distinguish lane markings from the extracted road surface in the LiDAR point cloud. Then, non-lane marking points among the extracted high intensity points are identified and removed. Next, the lane marking centerline is derived for lane width estimation.

Several data collection missions have been conducted in this study. To ensure the acquisition of an accurate point cloud, the calibration procedure was applied first and the generated LiDAR point cloud was used for lane width estimation. Various experimental setups are used in order to evaluate the performance of the proposed calibration strategy as well as the lane width estimation approach. First, the performance of the proposed calibration strategy is evaluated through the a-posteriori variance factor of the least squares adjustment (LSA) procedure and the quality of fit of the adjusted point cloud to planar surfaces and linear features before and after the calibration process. Then, to demonstrate the feasibility and performance of the proposed lane width estimate approach, a comprehensive testing is conducted with six datasets collected in different seasons and using different sensors. The first experiment shows the importance of accurate estimates of mounting parameters for identification of lane markings and lane width estimation. The second demonstrates the compatibility of estimated lane width from two different types of spinning multi-beam laser scanners. The third indicates the accuracy of calibration results and the precision of lane width estimates by comparing the results obtained from five datasets for two road segments (with a total length of approximately 30 miles) scanned by different sensors in different seasons. The last experiment demonstrates the accuracy of lane width estimates by comparing the results obtained for a test dataset collected for a road segment with those derived from manually digitized lane markers and on-site manual measurements. These experimental results indicate that the proposed strategy can provide lane width estimates that are precise to around 2 cm and have an accuracy of about 3 cm.

Findings

- When the mounting parameters are inaccurate, the derived point cloud would be distorted. In this case, precise lane width estimates cannot be derived. Although the lane width estimation strategy includes outlier removal and LSA-based line fitting that can minimize the effect of inaccurate mounting parameters, it cannot mitigate the effects altogether.
- The lane widths derived from HDL32E and VLP16 laser scanners are found to be compatible. However, VLP16 generates more sparse points than HDL32E, which would cause incomplete centerline extraction. In case of curved road segments, incomplete centerline extraction would result in inaccurate lane width estimation. Therefore, in order to avoid the discrepancies caused due to the sparse nature of point cloud acquired from VLP16, it is recommended to have slower driving speed during (e.g., 25 miles/hour) data collection.
- The lane width estimates for two road segments from five different datasets are derived, and the results demonstrate that the precision of the proposed lane width estimation strategy can range from 1 cm to 3 cm.
- The accuracy of lane width estimates is evaluated by comparing the results obtained for a test dataset collected for a road segment with those derived from manually digitized lane markers and on-site manual measurements (ground truth). The difference between the derived lane width estimates using the proposed strategy and ground truth is 3.04 cm, which validates the accuracy of the lane width estimates from the proposed strategy and also indicates the accuracy of mounting parameter estimates from the system calibration. Also, the difference between the lane width obtained from the manually digitized centerline and ground truth is around 1.31 cm, which again illustrates the accuracy of mounting parameter estimates.

Implementation

Data Collection

The first step in the process of data collection is to mount the mapping system onto a mobile platform (here, a car) and test the operation of the different equipment in order to avoid any technical glitches during the course of data collection. The setup of MMS takes about 30 minutes. As discussed before, each data collection is preceded by a calibration dataset collection for which the calibration targets are set up in an outdoor environment, which is accomplished in another 30 minutes. It is followed by

5 minutes of dynamic alignment of the GNSS/INS unit, and then a total of approximately 10 minutes of drive-runs at an average speed of 4 miles per hour around the calibration test field. After that, work zone data is ready to be collected and needs to be monitored. The driving speed is around 40 miles per hour for work zone data collection. Finally, the data collection is ended with another dynamic alignment of the system for 5 minutes.

Data Processing

3D Point Cloud Reconstruction

The first and foremost step for 3D point cloud reconstruction is the processing of GNSS/INS data to generate the navigation dataset using the post-processing software provided by NovAtel or Applanix (depending on the GNSS/INS unit used), which takes about 30 minutes. The Velodyne laser units store the captured data in PCAP format that needs to be decoded to extract useful information about the scanned points; it is used along with the navigation data and initial estimates of mounting parameters to reconstruct an initial 3D point cloud (in *.las format). The time taken to reconstruct the PCAP files depends on the amount of data collected and the number of threads used during reconstruction (i.e., the number of PCAP files that are simultaneously reconstructed). For instance, a mission of 2.5 hours will result in a total of about 82 PCAP files, which would take a total of approximately 1.5 hours for reconstruction with five threads.

System Calibration

After reconstruction, the mounting parameters of MMS are calibrated in order to be able to obtain a point cloud with higher positional accuracy. First, the navigation data is used to extract the beginning and ending times for each of the parallel drive-runs around the calibration targets. Next, the point cloud captured in each drive-run is stored as a separate *.las file. These files are used to carry out a semi-automatic conjugate feature extraction process for calibration by determining seed points for highly reflective sign boards and checkerboards, diagonally opposite corners of ground/ wall patches, and end points of linear features. The track separation and feature extraction can be achieved in a total of about 1 hour. Next, the extracted conjugate features are used as input for calibration (which takes about 10 minutes), thus resulting in accurate estimates of mounting parameters.

Lane Width Estimation

Having accomplished a successful calibration, all the PCAP files (raw laser scanning measurement) are again reconstructed using the new accurate estimates of mounting parameters to generate revised *.las files (point clouds) that can be used for lane width estimation. In order to estimate lane width, first the road surface is extracted, which takes from 30 minutes to 1 hour. Next, the high intensity points representing the lane markings are extracted from the road surface in 5 minutes. Then, the navigation data is used along with the high-intensity points to derive the lane marking centerline, which requires 10 minutes. Finally, the derived centerlines from opposite sides of the road are separated out and used to derive the lane width estimates, which takes about 10 minutes. Based on these time estimates for each step, the total data processing time for any collected dataset can be estimated.

CONTENTS

LIST OF TABLES

LIST OF FIGURES

1. INTRODUCTION

Road digital maps including road characteristics (e.g., lane marking, lane width, slope, curvature, clothoid, shoulder width, and shoulder barriers) are useful for driver assistance systems, road safety inspection, traffic accident reduction, and infrastructure monitoring. The road characteristics are more critical in work zones since the lanes in such areas undergo very frequent alterations over the lifetime of a project, thus increasing the rate of accidents (Ozturk, Ozbay, & Yang, 2014). Federal Highway Administration (FHWA) reported that there were an estimated 96,626 accidents at work zones in 2015, out of which 642 accidents involved at least one fatality (FHWA, n.d.). Efficient work zone monitoring and inspection is one of the critical tasks to decrease traffic accidents. Lane width is an important aspect for road safety inspection in work zones. When a lane is narrow, it would result in a reduced roadway capacity, which would lead to traffic congestion and also, increase the probability of severe accidents. Moreover, the lane capacity in work zones is drastically less than that in non-work zone areas with the same lane width, as shown in Figure 1.1 (Mekker et al., 2018), which indicates, for instance, a reduction of 900 vehicles per hour for a 12 ft lane from HCM 2010. In work zones that have low capacity, a lane width reduction of 1 ft (30.48 cm) would result in decrease of 100 vehicles per hour per lane, thus leading to a severe congestion. Therefore, an accurate estimation of lane width is necessary. However, collecting geospatial data in work zones should consider the following aspects:

1. Manual on-site data collection is an expensive, time-consuming, and labor-intensive task. Moreover, it can expose field crew to dangerous road traffic.

2. To the best of authors' knowledge, there is no open source GIS database, such as OpenStreetMap, that consists of lane width information in work zones.
3. Scheduling airborne image collection missions at the required high frequency for monitoring work zones would be expensive. Moreover, the logistics and deployment of platforms/sensors for the mission on time might not be possible.
4. High-resolution satellites may not be able to capture data over work zone areas at sufficiently frequent time intervals. Furthermore, traffic conditions might hinder lane width estimation.
5. Due to the short lifetime of construction projects and continuous alteration of lanes, open source GIS data and satellite images may not be able to provide up-to-date information for work zones.

Using mobile mapping systems (MMS) equipped with Light Detection and Ranging (LiDAR) units and cameras, geo-referenced point clouds and images can be collected rapidly in work zones without affecting traffic. Then, road characteristics can be derived from the acquired point cloud for risk assessment. This report first introduces multi-unit LiDAR system calibration procedure for deriving point cloud with high positional accuracy and then, discusses the lane width estimation approach using LiDAR point cloud acquired from a calibrated MMS.

The remainder of this report presents the proposed framework in more detail. First, a literature review of existing approaches for MMS calibration and road feature extraction are presented in Chapter 2. Then, an overview of the mobile mapping system used in this research is introduced in Chapter 3. Next, the conceptual basis of LiDAR point positioning is discussed in Chapter 4. In Chapter 5, the proposed calibration procedure of a mobile mapping system comprising several spinning
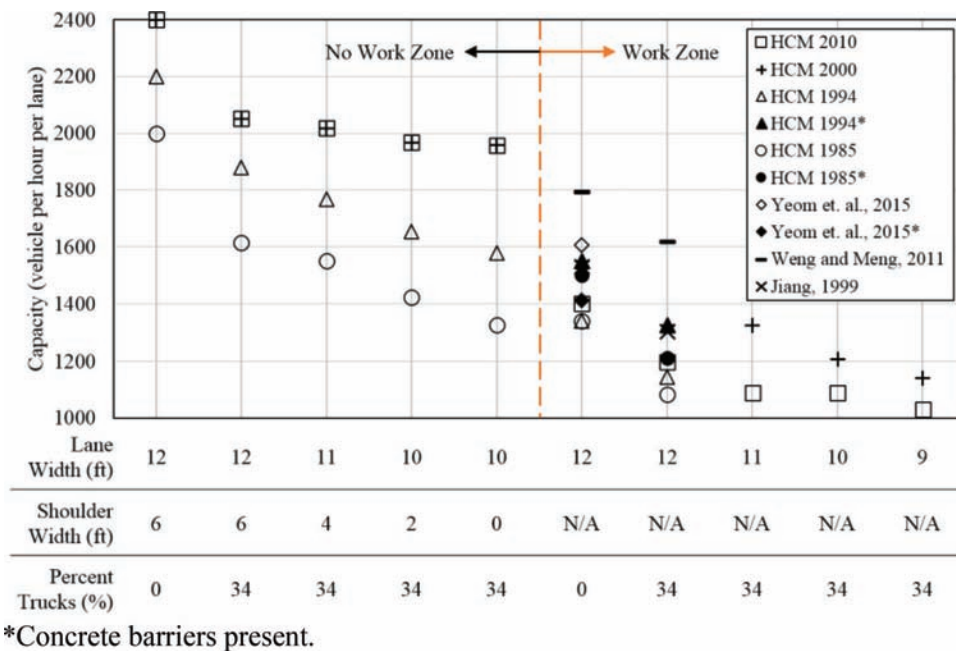
Figure 1.1 Summary of freeway capacity estimation for different scenarios (Mekker et al., 2018).

multi-beam laser scanners (i.e., Velodyne laser scanners) and GNSS/INS unit is delivered. Moreover, the performance of the proposed calibration strategy is evaluated through the a-posteriori variance factor of the LSA procedure and the quality of fit of the adjusted point clouds to the best-fitted model before and after the calibration process. After deriving an accurate point cloud, the proposed lane width estimation strategy is discussed in Chapter 6. Additionally, four validation methodologies for the proposed lane width estimation strategy are provided: (1) investigating the impact of the estimated mounting parameters from multi-unit LiDAR system calibration on the identification of lane markings and derived lane width estimates; (2) comparison of results from two types of laser scanners; (3) analysis of multiple datasets collected over the same test area to demonstrate the precision of estimated lane width and reliability of the introduced calibration approach; and (4) comparison with on-site manual measurements and manually digitized lane markers to show the accuracy of estimated lane width. After the discussion of the proposed strategies and experimental results, an implementation overview is described in Chapter 7. Finally, the report concludes with a summary of the characteristics of this study and provides recommendations for future work in Chapter 8.

2. LITERATURE REVIEW

Mobile mapping systems are able to rapidly acquire geo-spatial data pertaining the environment within which they are deployed. MMSs were developed in the late 1980s and early 1990s (Ellum & El-Sheimy, 2002; Novak & Bossler, 1995; Puente, González-Jorge, Martínez-Sánchez, & Arias, 2013). In the early stage, MMSs usually carried a set of optical cameras and a geo-referencing system (i.e., integrated Global Navigation Satellite Systems and Inertial Navigation Systems—GNSS/INS), which is capable of providing accurate position and orientation of the platform at high frequency (Schwarz & El-Sheimy, 2007). With the emergence of laser scanners, modern MMSs usually carry both laser scanners and optical cameras as well as a geo-referencing system. Laser scanners onboard airborne and terrestrial platforms have been established as a proven technology for the acquisition of dense point clouds with high positional accuracy. The main factors behind the widespread use of LiDAR systems include the ever-continuous improvement in GNSS/INS direct geo-referencing technology as well as enhanced performance and reduced size and cost of laser scanning units. Currently, there are commercially available LiDAR units that are capable of emitting more than a quarter million pulses per second at a cost of less than $10k. Such availability, together with the ever-increasing range of applications—such as Digital Building Model generation, transportation corridor monitoring, telecommunications, precision agriculture, infrastructure monitoring, seamless outdoor-indoor mapping, and power line clearance evaluation (Lin et al., 2013; Puente et al., 2013; Weiss & Biber, 2011; Williams, Olsen, Roe, & Glennie, 2013)—have

led to the development of multi-unit mobile LiDAR systems onboard airborne and terrestrial platforms that are either manned or unmanned. However, the attainment of the full positioning potential of such systems is contingent on an accurate calibration of the mobile mapping unit as a whole. Therefore, calibration of the system is a necessary step and the previous research in this field is discussed in section 2.1. After calibrating the mobile mapping system, an accurate 3D point cloud can be reconstructed to derive useful information along the road surface (e.g., road surface extraction, lane marking identification, characteristics of roads) and the progress in this domain is briefly described in section 2.2.

2.1 Calibration of Mobile Mapping Systems

The calibration of MMSs to estimate the mounting parameters relating the different components, such as laser scanners, cameras, and GNSS/INS unit, is the foremost step to get the full positioning potential of MMSs. Habib, Kersting, Shaker, and Yan (2011) studied the impact of airborne LiDAR system calibration on the relative and absolute accuracy of the derived point clouds, both qualitatively and quantitatively. The relative accuracy was evaluated by quantifying the degree of co-alignment of overlapping strips before and after calibration, whereas the absolute accuracy was evaluated by quantifying the degree of compatibility between LiDAR and control surfaces before and after calibration. This report proposes a multi-unit LiDAR system calibration strategy for a mobile terrestrial platform, which can be used to directly estimate the mounting parameters relating spinning multi-beam laser scanners to the onboard GNSS/INS unit.

The cost-effective Velodyne laser scanner, which is a spinning multi-beam laser unit and can rapidly capture a high volume of data, has been used in many mobile mapping systems and robotics applications (Choi, 2014; Schwarz, 2010; Vallet, Xiao, & Brédif, 2015). Over the past few years, a great deal of research has been devoted to modeling the inherent systematic errors in Velodyne laser scanners as well as the calibration of LiDAR systems (Atanacio-Jiménez et al., 2011; Glennie et al., 2013). Underwood, Hill, and Scheding (2007) calibrated the extrinsic parameters relating a SICK LMS-291 to a NovAtel Synchronized Position Attitude Navigation (SPAN) system by minimizing the discrepancy between sensed data and a known structure (i.e., a vertical pole and relatively flat ground). Muhammad et al. (2010) performed calibration of a rotating multi-beam LiDAR with the objective for aligning the scan data as close as possible to a ground truth environment. He, Zhao, Davoine, Cui, and Zha (2013) used pairwise multi-type 3D geometric features (i.e., point, line, plane) to derive the extrinsic parameters between 2D LiDAR and GPS/IMU. First, the points are segmented into different features and their quality is evaluated to compute weights to be used in the minimization of normal distance between conjugate features. However, when the initial

parameters are considerably inaccurate, the segments and derived weights may not be reliable. Chan, Lichti, and Belton (2013) introduced an intrinsic parameters calibration for Velodyne HDL-32E based on static stations and also analyzed the temporal stability of range measurements which indicated an approximate warm-up time of 2000 sec for most laser beams. Glennie, Kusari, and Facchin (2016) performed a geometric calibration with stationary VLP-16 to marginally improve the accuracy of the point clouds by approximately 20%. Moreover, they also investigated the range accuracy of VLP-16, which is quoted to have an RMSE value between 22 to 27 mm in the factory supplied calibration certificate. But, it was observed that some of the laser beams have worse range accuracy than others. Although many LiDAR system calibration procedures have been developed in the past, outdoor calibration of integrated GNSS/INS and multi-unit 3D laser scanners is still an active area of research.

This research focuses on a potential calibration technique for a LiDAR system with several spinning multi-beam laser scanners onboard a terrestrial mobile mapping vehicle. The focus of the system calibration is to simultaneously estimate the mounting parameters relating the different system components by minimizing the discrepancy between conjugate linear and/or planar features in overlapping point clouds derived from different drive-runs. More specifically, the lever arm and boresight angles relating the individual laser scanners and the onboard GNSS/INS unit are derived using an iterative calibration procedure.

2.2 Extraction of Road Characteristics

Mobile mapping systems can be used to acquire various road characteristics (e.g., lane marking, lane width, slope, curvature, clothoid, shoulder width, and shoulder barriers) which are crucial factors for building road digital maps, autonomous vehicle navigation, work zone monitoring, and road safety inspection. Imagery captured from MMSs can provide color information which would ease the detection of features of interest along a road surface. To detect roads/lane markings from imagery, the localization of road borders or lane markings is one of the commonly used approaches (Kong et al., 2010). Wang, Hu, Chen, and Zhang (2017) tracked and detected road lanes using change in the gradient and shape of a lane (i.e., the perspective effect on parallel lines). Lipski et al. (2008) utilized local histograms to detect lane marking features from Hue, Saturation, Value (HSV) top view images. Then, a lane fitting algorithm was carried out to find a parameter set for a lane model, i.e., the width and gradient of each of the connected lane segments within the model. The difficulty in feature extraction from imagery depends on illumination conditions, camera exposure, obstacles, and shadows. Hence, this report only focuses on feature identification and extraction from LiDAR point clouds.

Before deriving the road characteristics, road surface should be located and identified first. Han, Kim, Lee,

and Sunwoo (2012) detected road boundaries and obstacles by extracting line segments from the raw point cloud in polar coordinates and classifying those into road and obstacle segments by analyzing the change in roll and pitch angles of each segment. Kang, Rob, Suh, and Song (2012) used Hough transform to detect curb positions. Then, two Kalman filters were applied to track the curb using a prediction model. At the end, a probabilistic decision-making algorithm is applied to accurately estimate the roadside curb position. Zhang (2010) collected 3D point clouds with an LMS-200 SICK sensor mounted on top of a vehicle to detect road surface and road surface edges by analyzing the change in elevation. First, candidate road segments are extracted from the elevation data using a local-extreme-signal detector to identify the road surface edge. Then, the candidate road segment is given a weight based on the standard deviation of elevation and then, classified using linear Support Vector Machine (SVM) to decide whether the candidate is a road segment or not. Finally, the curb is detected when the side of curb is perpendicular to the road segment. Kumar, McElhinney, Lewis, and McCarthy (2013) utilized a Riegl VQ-250 laser scanner and an IXSEA LandINS GNSS/INS onboard an MMS to collect point clouds and extract road surfaces using a combination of two modified versions of the parametric active contour or snake model. The snake model was initialized based on the navigation information obtained from the GNSS/INS.

Transportation agencies apply highly reflective glass beads to lane markings to improve their visibility at night. Therefore, well-maintained retro-reflective lane markings along the extracted road surface will be manifested as high intensity points in LiDAR point cloud. Although the material used for road markings can provide high-intensity return, the reflected laser pulse intensities fluctuate strongly according to the incident angles and range between the laser beam firing point and its footprint. Kumar, McElhinney, Lewis, and McCarthy (2014) used a set of range-dependent thresholds to extract lane markings. First, the road surface was extracted and divided into blocks along the driving direction based on lateral distance from the navigation data representing the trajectory. Then, different thresholds were applied to different blocks for road marking extraction. Finally, morphological operations and generic knowledge of the dimensions of road markings were applied to complete the shapes of extracted road markings and remove noise. Yu, Li, Guan, Jia, and Wang (2015) proposed a multi-segment threshold to mitigate the effects of intensity variation of point clouds acquired from Riegl VMX-450. First, road surface was partitioned into blocks along the trajectory direction and then, each block was partitioned into a set of segments according to the lateral distance from the trajectory. Road markings in each segment were detected using Otsu's thresholding algorithm. Wrongly classified points were recognized and removed by calculating their local point density. Finally, road marking points were classified into specific categories using the following steps: (1) Euclidean distance grouping,

(2) voxel-based normalized cut segmentation strategy for dividing a group including several types of markings, and (3) marking classification using trajectory information, deep learning models, and Principal Component Analysis (PCA). Guan et al. (2014) collected point clouds from a Riegl VMX-450 MMS system and extracted lane markings using multiple thresholds. First, a curb-based strategy that relies on navigation data was applied to extract points belonging to the road surface by detecting elevation change along the road profile. Next, points representing road surface were interpolated into a geo-referenced intensity image. Then, road markings were segmented using multiple thresholds that correspond to different ranges as determined by point density. Finally, a morphological operation was applied to complete the shape of road marking and remove noise.

Cai and Rasdorf (2008) modeled road centerlines and predicted their length using LiDAR and planimetric road centerline data. The LiDAR data (with a point density of approximately 0.031 pts/m^2) was obtained from North Carolina Floodplain Mapping Program and the planimetric road centerline data was obtained from the GIS unit of the North Carolina Department of Transportation (NCDOT). A snapping and interpolation approach was used to obtain 3D points along road centerlines. Holgado-Barco, González-Aguilera, Arias-Sanchez, and Martinez-Sanchez (2014) used PCA to analyze point clouds captured from an Optech LYNX mobile mapper for deriving road parameters (i.e., slope, vertical curves, and superelevations) from segmented cross-sectional road surface extracted with the help of trajectory and setting scan-angle threshold. The slope and superelevation were computed using PCA for each road segment. After deriving the slope, characteristics of vertical curves were estimated. Holgado-Barco, González-Aguilera, Arias-Sanchez, and Martinez-Sanchez (2015) extracted lane markings and derived the geometric design of a road (i.e., curvature and azimuth). First, lane marking points were extracted by setting intensity and scan-angle thresholds and the points were segmented every 0.5 m using their time-stamps. The centroid of each segment was regarded as a point along the lane marking centerline. Next, the lane marking centerline was used to derive their azimuth for checking the horizontal alignment and curvature of the road. Wang, Teoh, and Shen (2004) estimated road slope and superelevation using point clouds from an Optech Lynx SG1 system. First, the road surface was segmented and partitioned into blocks along the driving direction using navigation data. Then, the points from a road surface partition were used to derive the slope and superelevation.

None of the above research considers lane width estimation, which is one of the key factors in road safety inspection. Also, none of these approaches dealt with the architecture of the used mobile mapping system and laser scanners, and their impact on lane width estimation and road segment characterization. The system calibration of MMSs and its impact on derived lane width estimates is also an issue that has not been addressed. Moreover, most of these studies validate the results only once for a single test area. In this report, an outdoor multi-unit LiDAR calibration procedure is introduced. Then, the proposed lane width estimation strategy is applied to derive the lane width using point clouds acquired by the calibrated MMS.

3. SYSTEM ARCHITECTURE OF THE MMS USED IN THIS RESEARCH

3.1 System Specifications and Synchronization

The test datasets used in this research are captured by a designed mobile mapping platform, which includes a Velodyne VLP-16 laser scanner, Velodyne HDL-32E laser scanner, FLIR Flea-2G camera, and SPAN-CPT GNSS/INS, as shown in Figure 3.1. The HDL-32E consists of 32 radially oriented laser rangefinders that are aligned from +10.67° to -30.67°. In total, the vertical field of view (FOV) is 41.34°. Also, the whole unit can rotate to achieve a 360° horizontal FOV. The point capture rate is around 700,000 points per second (Velodyne, 2016a). The VLP-16, that has 16 radially oriented laser rangefinders, is a lite version of the HDL-32E. The vertical FOV is from -15° to +15° and the horizontal FOV is 360°. The point capture rate is around 300,000 points per second (Velodyne, 2016b). The navigation system adopted in this research is the SPAN-CPT that combines GNSS and Inertial Measurement Unit (IMU) hardware inside a single enclosure. The GNSS collection rate is 20 Hz and the IMU measurement rate is 100 Hz (NovAtel, 2014). The FLIR Flea-2G camera is used as an auxiliary sensor in this study and is directly georeferenced by the SPAN-CPT unit. The FLIR Flea-2G camera has a maximum image resolution of 5 MP and has built-in ports for both triggering and strobe feedback signals.

In order to derive a directly georeferenced LiDAR point cloud, the SPAN-CPT supplies sequentially precise time pulses, known as pulse-per-second (PPS) signals, which gives the ability to generate a time-tagged point cloud. Furthermore, the SPAN-CPT provides a navigation message, also known as the "GPRMC" message (including information related to position, rotation, and GPS time), which is transmitted over a dedicated RS-232 serial port and is received by the LiDAR unit via the Velodyne interface box in the form of serial data. This synchronization process is illustrated in Figure 3.2.

The accuracy of the derived LiDAR point cloud from the utilized platform through error propagation can be estimated. The SPAN-CPT can attain an accuracy of less than 2 cm in position, and an accuracy of 0.008° and 0.035° in the roll/pitch and heading, respectively (NovAtel, 2014). The Velodyne laser unit has a range accuracy of 2 cm. These values, along with the nominal standard deviation of the estimated system mounting parameters, are used to derive the expected accuracy in the computed mapping frame coordinates using the LiDAR Error Propagation calculator developed by Habib et al. (2006), as shown in Figure 3.3. The calculator suggests that we should expect an accuracy of around 2–3 cm at a range of 30 m. Since the accuracy of lane width estimates would directly depend on the LiDAR point cloud accuracy, the accuracy of derived lane width can be expected around 3 cm.

3.2 Portability of the Used MMS

The designed mapping system for this research is highly portable. Firstly, it can be easily mounted on different mobile platforms, such as cars or trucks. The initial deployment time is usually around 30 mins. Moreover, the mapping system is also flexible in terms of the involved components (laser scanners and cameras),

Figure 3.1 Mobile mapping system used in this research.
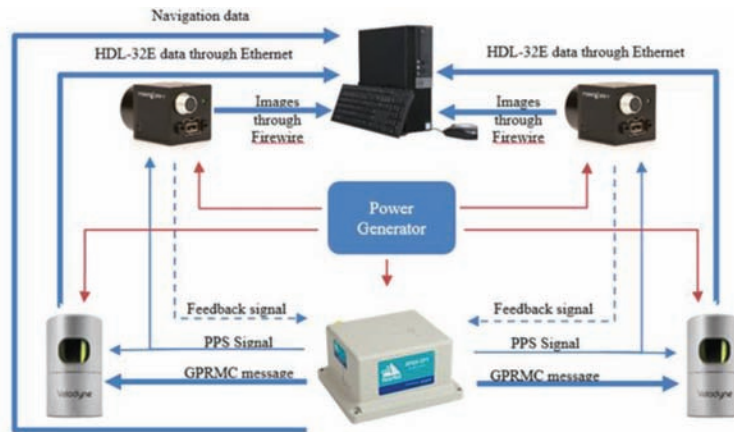
Figure 3.2 Synchronization process and data storage for the mobile mapping system.

Figure 3.3 LiDAR Error Propagation calculator.

i.e., these units are detachable and can be easily replaced with an alternate unit. Note that in all such circumstances, the MMS needs to be re-calibrated in order to account for any subtle or significant change in mounting parameters. Some instances of deployment of the MMSs are shown in Figure 3.4.

Figure 3.4 Example deployments of the MMS.

4. CONCEPTUAL BASIS OF LIDAR POINT POSITIONING

4.1 Single LiDAR Unit Point Positioning

A typical LiDAR system consisting of a spinning multi-beam LiDAR unit could involve 3 coordinate systems (i.e., mapping frame, IMU body frame, and laser unit frame). A given point, I, acquired from a mobile mapping system can be reconstructed in the mapping coordinate system using Equation 4.1, which is graphically illustrated in Figure 4.1. The vector and matrix notations used in this report are as follows:

- r_a^b denotes the coordinates of point 'a' relative to point 'b' in the coordinate system associated with point 'b'.

- R_a^b denotes the rotation matrix that transforms a vector defined relative to the coordinate system 'a' into a vector defined relative to the coordinate system 'b'.

For the laser unit frame of a spinning multi-beam laser scanner, origin is defined at the laser beam firing point and the z-axis is along the axis of horizontal rotation of the laser unit. For a Velodyne system, each laser beam is fired at a fixed vertical angle, α; the horizontal angle, β, is determined based on the rotation of unit; and the range, ρ, is defined by the distance between firing point and its footprint. So, the coordinates of a 3D point relative to the Velodyne laser-unit coordinate system, $r_I^{lu}(t)$, is defined by Equation 4.2. An IMU body frame should be considered when mobile systems are
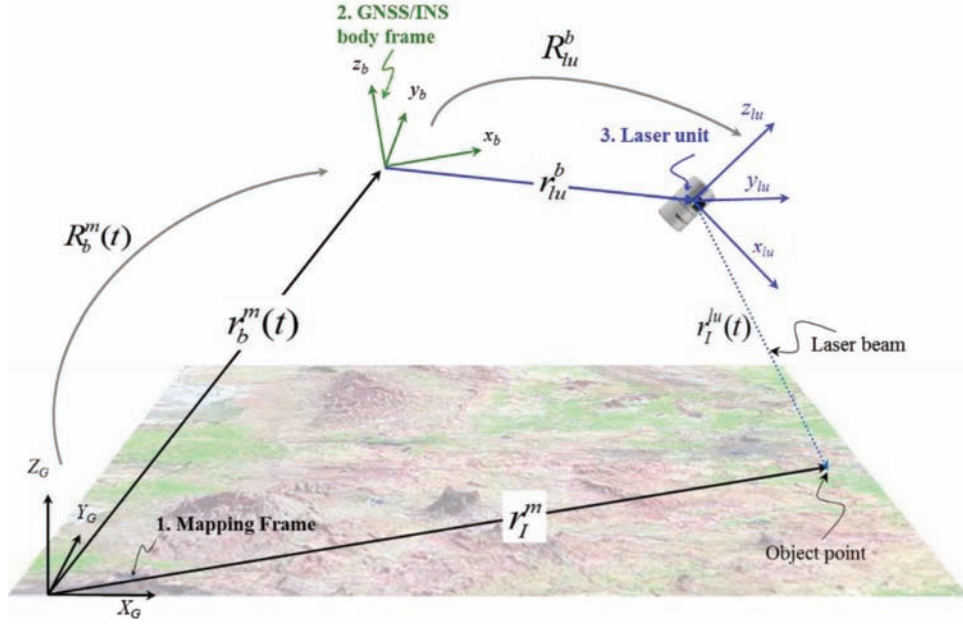
Figure 4.1 Illustration of point positioning of a directly geo-referenced single-unit LiDAR system.

equipped with a GNSS/INS navigation unit. For mobile systems, the lever arm, r_{lu}^b, and boresight matrix, R_{lu}^b, between laser unit and body frame coordinate systems is rigidly defined. The GNSS/INS integration provides the time dependent position, $r_b^m(t)$, and rotation, $R_b^m(t)$, relating the mapping frame and IMU body frame coordinate systems, according to the optimized solution from all the available GNSS and inertial measurements.

$$r_I^m = r_b^m(t) + R_b^m(t)r_{lu}^b + R_b^m(t)R_{lu}^b r_I^{lu}(t) \qquad (4.1)$$

$$r_I^{lu}(t) = \begin{pmatrix} x \\ y \\ z \end{pmatrix} = \begin{pmatrix} \rho(t)\cos\alpha(t)\cos\beta(t) \\ \rho(t)\cos\alpha(t)\sin\beta(t) \\ \rho(t)\sin\alpha(t) \end{pmatrix} \qquad (4.2)$$

4.2 Multi-LiDAR Unit Point Positioning

In case of a multi-unit LiDAR system, the points captured using each of the laser scanners can be reconstructed using Equation 4.1 with the mounting parameters relating each laser unit directly to the GNSS/INS navigation unit. An alternative approach for 3D point cloud reconstruction using a multi-unit LiDAR

system is provided in Equation 4.3, where a reference sensor and slave sensors are considered. An illustration of such a multi-unit LiDAR system is shown in Figure 4.2. In Equation 4.3, the terms r_{lur}^b and R_{lur}^b are the lever arm and boresight matrix, respectively, relating the IMU body frame and the reference laser unit coordinate systems. The extra terms considered in Equation 4.3, r_{luj}^{lur} and R_{luj}^{lur} are the lever arm and boresight matrix, respectively, rigidly relating the reference sensor, *lur*, and the slave sensor, *luj*. One can introduce one or more slave sensors, each one of them rigidly related to the reference sensor by a lever arm and boresight matrix.

$$r_I^m = r_b^m(t) + R_b^m(t)r_{lur}^b + R_b^m(t)R_{lur}^b r_{luj}^{lur}$$
$$+ R_b^m(t)R_{lur}^b R_{luj}^{lur} r_I^{luj}(t) \qquad (4.3)$$

Here, the model relating a reference sensor to the IMU body frame and the other slave sensors to the reference sensor is preferred over the model where each sensor is individually related to the IMU body frame. This is due to the fact that the former model allows to derive the mounting parameters relating the slave sensors to the reference sensor without the need for GNSS/INS position and orientation information, thus facilitating an indoor calibration for the mobile mapping system.
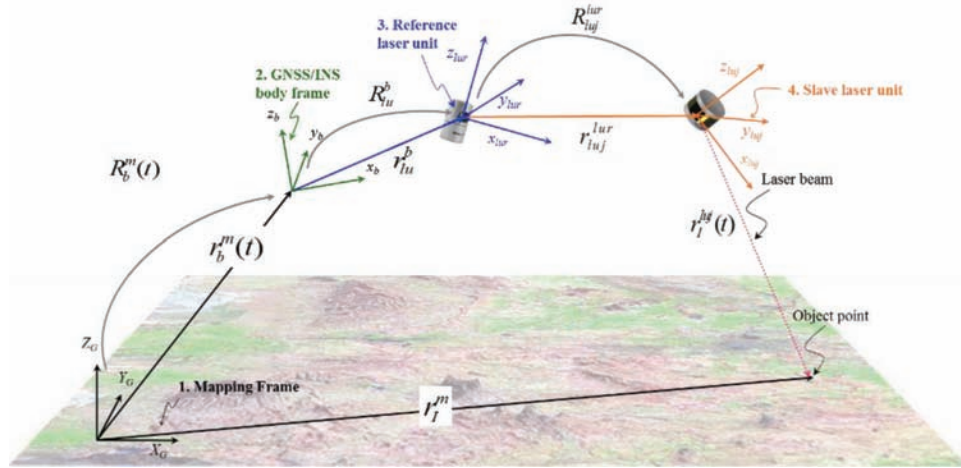
Figure 4.2 Illustration of point positioning of a directly geo-referenced multi-unit LiDAR system.

5. PROPOSED MULTI-UNIT LIDAR SYSTEM CALIBRATION PROCEDURE

5.1 Methodology of Proposed Multi-unit LiDAR System Calibration Procedure

In this section, we propose a strategy to estimate the mounting parameters using geometric tie features (e.g., planar, and linear/cylindrical features). The conceptual basis for multi-unit LiDAR system calibration is to minimize the discrepancies among conjugate points, linear features, and/or planar features obtained from different sensors and/or drive-runs. After collecting data from several drive-runs, a 3D point cloud relative to a global reference frame will be derived using the GNSS/INS unit position and orientation, and initial estimates for the mounting parameters. Then, conjugate features are identified and extracted from the reconstructed point cloud. Finally, an iterative multi-unit system calibration with weight modification is proposed to derive the mounting parameters based on the minimization of normal distance between conjugate features.

5.1.1 Representation Scheme and Feature Extraction

Owing to the irregular distribution of LiDAR points, conjugate point pairs cannot be used since there is no accurate point-to-point correspondence. Instead, conjugate linear/cylindrical and planar features, such as building façades, ground patches, light poles, flag poles, and lane markers, are used and these can be directly extracted from overlapping areas within the drive-runs. However, conjugate feature extraction from several drive-runs could be time-consuming and inefficient, especially when the initial estimates for mounting parameters used to reconstruct the 3D point cloud are considerably inaccurate. To facilitate automated identification of conjugate features in such cases, specifically designed calibration boards covered by highly reflective surfaces, that could be easily deployed and set up in outdoor environments, are used in this study, as shown in Figure 5.1. The representation scheme and extraction of various

Figure 5.1 Calibration test field.

linear and planar features from LiDAR point cloud is discussed in the forthcoming subsections.

5.1.1.1 Linear Features. Any linear feature appearing in a LiDAR scan is represented by a sequence of pseudo-conjugate points lying along the feature. Here, the term "pseudo-conjugate points" refers to points that are not distinctly identifiable in different LiDAR scans but are known to belong to the same feature. Note that points along a linear feature are labeled the same, thus denoting that the points are indistinct in nature, i.e., the only identification of a point is by the feature that it belongs to and there is no assumption about having conjugate points among different LiDAR scans.

In outdoor calibration, various linear features can be extracted and used for calibration, such as flag poles, light poles, physical intersections of neighboring planar features, and so on. Features like flag poles or light poles are extracted from LiDAR data by manually specifying the two end points for each feature. A buffer radius is set to define a cylinder around the linear feature

Figure 5.2 Intensity data of a point cloud obtained from a single drive-run.

of interest, as shown in Figure 5.3. The buffer radius is determined based on the accuracy of initial estimates of the mounting parameters, i.e., a higher buffer radius value is used in case of highly inaccurate initial estimates, and vice-versa. Then, a line-fitting is done for the points lying within this cylindrical buffer and finally, the points that lie within a normal distance threshold from the best-fitting line are extracted. Moreover, points belonging to intersections of neighboring planar features are extracted by firstly, determining the best-fitting planes for each of the two planar surfaces. Then, their intersection line is determined and all the points lying within a normal distance threshold from this line are extracted.

5.1.1.2 Planar Features. Any planar feature appearing in a LiDAR scan is represented by a sequence of pseudo-conjugate points lying along the feature. Note that LiDAR points belonging to each planar feature will have the same labels (which is specific to the feature). In this study, we use highly reflective boards, ground patches, wall patches, and other surfaces as planar features for calibration. The highly reflective sign boards can be easily identified from intensity data, as shown in Figure 5.2, where the points belonging to these boards exhibit higher intensity values compared to other LiDAR points. Firstly, a pre-defined threshold is set to extract high-intensity points. To avoid the extraction of high-intensity points belonging to objects other than these boards, an approximate pre-set region is manually set as seed points for each board. Then, a distance-based region growing technique is adopted to group the high intensity boards. Finally, a plane-fitting is done for these points, and the points lying within a normal distance threshold from the best-fitting plane are extracted. Again, the normal distance threshold is determined based on the accuracy of initial estimates of the mounting parameters. Other planar features, such as ground patches, wall patches, or other planar surfaces, are extracted by manually defining two diagonally

opposite corners, as shown in Figure 5.3. A bounding box is constructed around the planar feature of interest by adding a buffer value (in X, Y, and Z directions) to the coordinates of diagonally opposite corners. Again, a plane-fitting is done for the points contained inside the box, and the ones lying within a normal distance threshold from the best-fitting plane are extracted.

5.1.2 Weight Modification and Multi-Sensor System Calibration

In the proposed calibration method, conjugate features are extracted from the point clouds of different sensors and several drive-runs. The mounting parameters of each sensor are derived by minimizing the discrepancies among conjugate features (lines/planes) in overlapping drive-runs. Each pairing between conjugate features will result in a misclosure vector, which would be random ($\vec{e}$) in case of a conjugate point pair, as given by Equation 5.1. However, a pairing between non-conjugate points along corresponding planar or linear/cylindrical features would additionally introduce a non-random component ($\vec{D}$) in the misclosure vector, as given by Equation 5.2. This ($\vec{D}$) would lie along the planar surface or along the linear feature/axis of cylinder, respectively, as illustrated in Figure 5.4. Therefore, a modified weight matrix, P', is introduced to eliminate the non-random component of the misclosure vector, $\vec{D}$, from the LSA cost function, as given by Equation 5.3 (Renaudin et al., 2011). To derive this matrix, a local coordinate system (UVW) is established first using the LiDAR points belonging to the reference LiDAR scan for the feature. The reference LiDAR scan for a feature is the one consisting of the highest number of points belonging to the feature, which in turn enhances the reliability of the derived local coordinate system. For linear/cylindrical features, the U axis is aligned
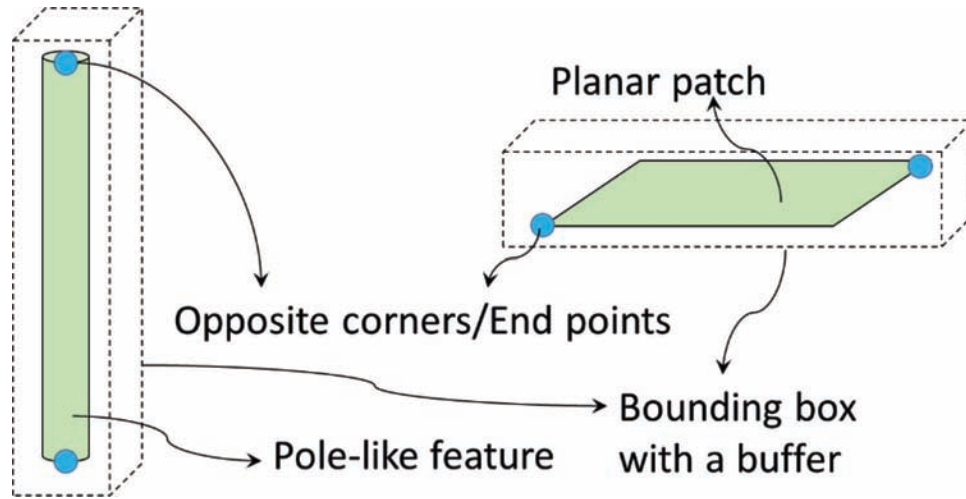
Figure 5.3 Illustration of semi-automatic feature extraction.
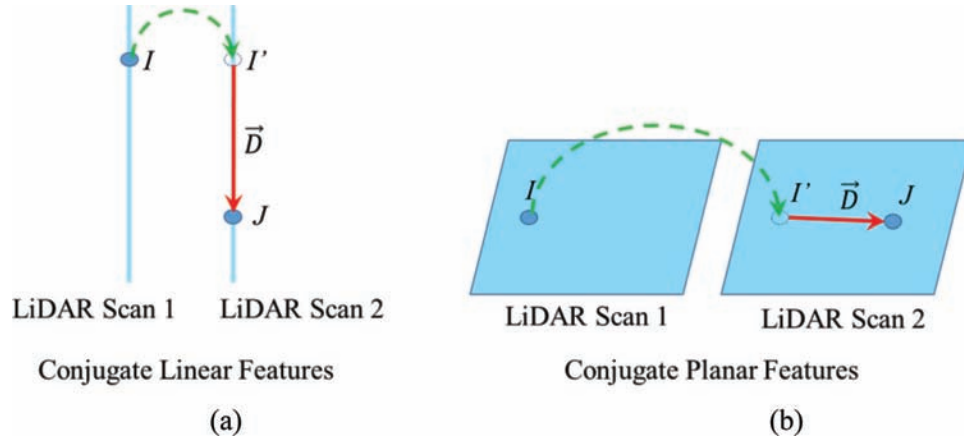
Figure 5.4 Discrepancy vector between non-conjugate points along corresponding (a) planar, and (b) linear features.
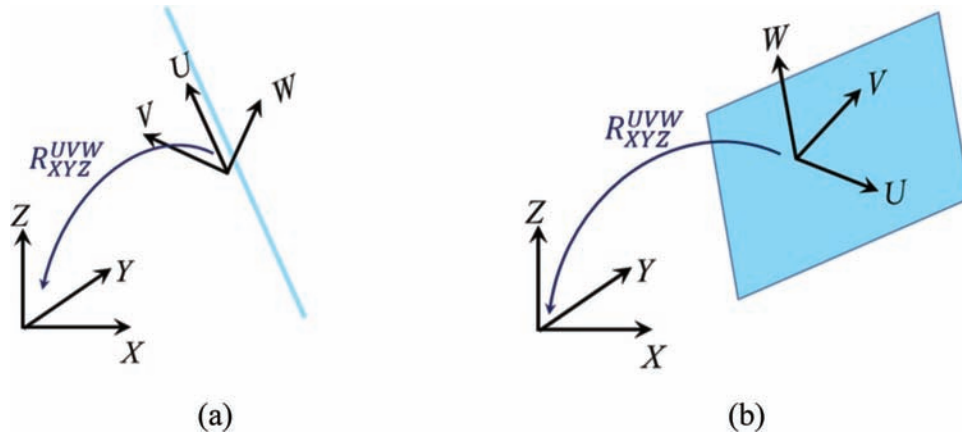
Figure 5.5 Illustration of local coordinate systems for (a) planar and (b) linear features.

along the line/axis of cylinder and V and W axes are arbitrarily chosen to satisfy the orthogonality of the UVW triad. For planar features, W axis is aligned along the normal vector of the plane in question, and U and V axes are arbitrarily chosen along the planar feature. An illustration of the local coordinate systems for the two types of features is shown in Figure 5.5. Then, a rotation matrix, R_{XYZ}^{UVW}, relating the local and mapping coordinate systems is derived according to the components of the vectors, U, V, and W relative to the mapping frame. The weight matrix, P_{XYZ}, in the mapping coordinate system is transformed to a weight

matrix, P_{UVW}, in the local coordinate system according to the law of error propagation (Equation 5.4). The weight matrix, P_{UVW}, is modified by assigning a zero weight to the elements corresponding to the direction of $\vec{D}$. More specifically, the non-random component of the misclosure vector $(\vec{D})$ can be eliminated from the LSA minimization target function by setting a zero weight in the corresponding direction. The direction of $(\vec{D})$ for a linear/cylindrical feature is along the U axis. Therefore, the modified weight matrix, P'_{UVW}, has zero weight in all the elements pertaining to the U axis (Equation 5.5). Similarly, the direction of $(\vec{D})$ for a planar feature is along the U and V axes. So, all the elements pertaining to the U and V axes are assigned a zero weight (Equation 5.6). The modified weight matrix, P'_{XYZ}, in the mapping coordinate system is derived using Equation 5.7. Finally, the obtained modified weight matrix, P'_{XYZ}, is applied to the condition in Equation 5.2 to account for pseudo-conjugate points along corresponding features within overlapping drive-runs.

$$Points: r_I^m(drive-run1) - r_I^m(drive-run2)\vec{e} \qquad (5.1)$$

$$Planar/LinearFeatures: r_I^m(drive-run1)$$

$$-r_J^m(drive-run2) = \vec{D} + \vec{e} \qquad (5.2)$$

$$P'\vec{D} = P'\begin{bmatrix} d_x \\ d_y \\ d_z \end{bmatrix} = 0 \qquad (5.3)$$

$$P_{UVW} = R_{XYZ}^{UVW} P_{XYZ} R_{XYZ}^{UVW} T$$

$$= \begin{bmatrix} P_U & P_{UV} & P_{UW} \\ P_{VU} & P_V & P_{VW} \\ P_{WU} & P_{WV} & P_W \end{bmatrix} \qquad (5.4)$$

Linear/Cylindrical Feature:

$$P'_{UVW} = \begin{bmatrix} 0 & 0 & 0 \\ 0 & P_V & P_{VW} \\ 0 & P_{WV} & P_W \end{bmatrix} \qquad (5.5)$$

$$PlanarFeature: P'_{UVW} = \begin{bmatrix} 0 & 0 & 0 \\ 0 & 0 & 0 \\ 0 & 0 & P_W \end{bmatrix} \qquad (5.6)$$

$$P'_{XYZ} = R_{XYZ}^{UVW} T P'_{UVW} R_{XYZ}^{UVW} \qquad (5.7)$$

5.1.3 Contribution of Point-Pairings toward System Calibration

Now, the contribution of pairings toward calibration is analyzed for linear features and planar features. One should note that each point pair serves two purposes—first is the derivation of 3D mapping frame coordinates of the involved points and second is the estimation of system calibration parameters. So, in order to determine the contribution from a pairing toward system calibration, we compute the point definition redundancy, i.e., the redundancy for the derivation of the 3D mapping frame coordinates of LiDAR points, as a result of LiDAR-to-LiDAR pairings. One should note that in case of a LiDAR point, there are no additional unknowns involved in computing its 3D mapping frame coordinates apart from the system parameters.

5.1.3.1 Linear Feature-Based Pairings. As discussed before, a linear feature is represented by a sequence of pseudo-conjugate points along the feature. Each pseudo-conjugate point pairing will result in a random misclosure vector $(\vec{e})$ along with a non-random misclosure vector $(\vec{D})$, as shown in Figure 5.4 (a) and expressed mathematically in Equation 5.2.

In this case, the discrepancy of the resultant point pair should be minimized only along the two directions that are normal to the axial direction of the linear feature, thus resulting in two equations from each pseudo-conjugate point pair. This is achieved by applying a modified weight matrix to the point pair which nullifies the component of their discrepancy along the axial direction of the linear feature. This modified weight matrix is derived according to the estimated direction of the linear feature based on the points from a reference LiDAR scan that belong to this feature (Renaudin et al., 2011). The scan consisting of most number of points belonging to a feature is set as the reference scan as it would result in the most reliable estimate of the feature direction.

Every sensor and every drive-run will give lead to a new version for each feature. For instance, a feature extracted from m different sensors and n different drive-runs will lead to mn separate versions for this feature. Then, there can be a total of $\frac{mn(mn-1)}{2}$ pairings for each feature. However, the discrepancy observations corresponding to these pairings will not be independent. Hence, in this research, one of the versions is selected as reference to be paired with all the other versions of that feature from other sensors and/or drive-runs. So, there would be $(mn-1)$ linearly independent LiDAR-to-LiDAR pairings for each feature. A pseudo-conjugate LiDAR-to-LiDAR point pairing will give 2 equations and no unknowns, thus leading to a point definition redundancy of 2.

5.1.3.2 Planar Feature-Based Pairings. A planar feature is also represented by a sequence of pseudo-conjugate points along the feature. Again, each pseudo-conjugate

point pairing will result in a random misclosure vector ($\vec{e}$) along with a non-random misclosure vector ($\vec{D}$), as shown in Figure 5.4 (b) and stated before in Equation 5.2. So, the discrepancy of the resultant point pair is minimized only along the direction normal to the planar surface, thus resulting in only one equation from each pseudo-conjugate point pair. Again, this is achieved by deriving a modified weight matrix by estimating the normal direction of the planar surface based on the points from the corresponding reference LiDAR scan that belong to this feature (Renaudin et al., 2011). This matrix would nullify the components of the discrepancy along the normal direction of the planar feature.

Let us consider a planar feature captured from m different sensors and n different drive-runs. Again, there will be a total of ($mn-1$) independent LiDAR-to-LiDAR pairings. A pseudo-conjugate LiDAR-to-LiDAR point pairing will lead to 1 equation and no unknowns, which implies a point definition redundancy of 1.

5.1.4 Implementation of the Proposed Iterative Calibration Strategy

In this section, we summarize the proposed strategy to simultaneously calibrate the mounting parameters of the spinning multi-beam laser scanners onboard a mobile platform using tie points and tie features (e.g., planar and linear features). After collecting data from several drive-runs/flight lines, a LiDAR-based 3D point cloud relative to a global reference frame will be derived using the GNSS/INS unit position and orientation, and initial estimates for the mounting parameters. Then, conjugate features are identified and extracted from the reconstructed point cloud. The mounting parameters for both reference and slave laser units can be derived by minimizing the discrepancies among the conjugate features arising from the pairings between the different versions of such features. However, when the initial estimate of mounting parameters is inaccurate, the initial point cloud would be inaccurate, as shown in Figure 5.6. Thus, the estimated modified weight matrix would be imprecise which would affect the accuracy of the derived mounting parameters. Hence, this research proposes an iterative calibration procedure. Firstly, the mounting parameters are derived through minimizing the discrepancies among extracted features through the weight modification process. Then, the points along the extracted features are re-generated using the newly estimated mounting parameters and the discrepancy among conjugate features is minimized again using a newly defined modified weight matrix. The above steps are repeated until the change in the estimates of the mounting parameters is below a predefined threshold.

The mounting parameters that are derived in multi-sensor calibration are the lever arm ($\Delta X, \Delta Y$) and boresight angles ($\Delta\omega, \Delta\phi, \Delta\kappa$) for all the sensors and the lever arm ΔZ for all but the reference sensor. The lever arm ΔZ for the reference sensor cannot be estimated in the calibration procedure since any change in ΔZ will not introduce discrepancies among the different versions of the same feature captured from different sensors and/or drive-runs. It would only result in a shift of the point cloud in the vertical direction as a whole. So, ΔZ for the reference sensor is fixed during the calibration procedure. It can either be manually measured or determined using vertical control (such as, horizontal planar patches with known elevation).

5.2 Experimental Results of Multi-unit LiDAR System Calibration

To illustrate the performance and feasibility of the proposed calibration strategy, three experiments are conducted in this section. The datasets used for evaluating the performance of the proposed calibration strategy are captured by a designed platform which carries either Velodyne HDL-32E or VLP-16 laser scanners together with a SPAN-CPT direct geo-referencing unit. In the first experiment, a calibration dataset is utilized to demonstrate the performance of the calibration strategy and the

Figure 5.6 Intensity data of a point cloud obtained from a single drive-run using inaccurate initial estimates of mounting parameters.
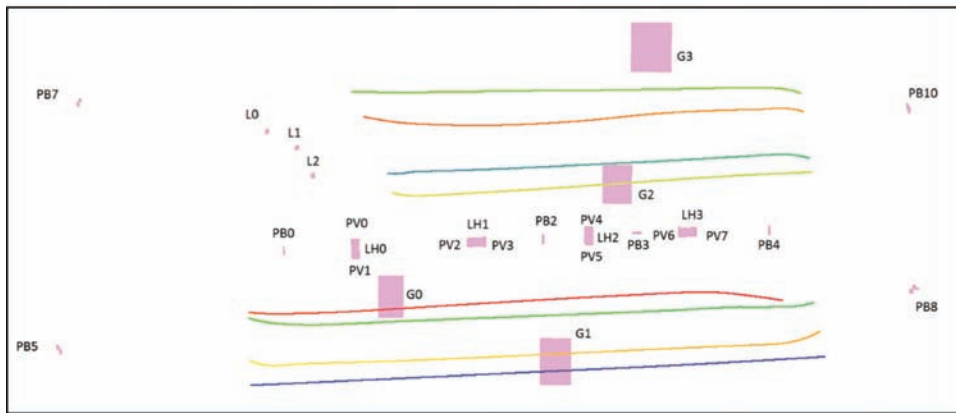
Figure 5.7 Calibration test field: (a) imagery, and (b) configuration of drive-runs and calibration primitives.

quantitative as well as qualitative results are provided. In the second experiment, a qualitative evaluation is provided by presenting objects from highway dataset to show the alignment between point clouds from drive-runs in different direction. In the third experiment, a repetitive testing is provided to show the feasibility of proposed calibration strategy. Mounting parameters were derived for the mobile mapping systems used to capture six datasets on different dates and using different sensors. Those six datasets would be used further for lane width evaluation in the next chapter.

5.2.1 Performance Evaluation from Calibration Dataset

For calibration dataset, specially designed hut-shaped target boards are also deployed, with their ridges oriented perpendicular to each other. These boards, along with the ground patches and light poles, would ensure enough control along all the directions (i.e., X, Y, Z-directions). In this experiment, eight drive-runs, with different directions and lateral distance between them, were made around the calibration primitives at an approximate speed of 4 miles/hr. With eight drive-runs and two laser units, there is a total of 16 versions

for each of the features used for the calibration procedure. Figure 5.7 (a) shows the calibration test field and Figure 5.7 (b) shows the configuration of drive-runs and target primitives, where PB denotes highly reflective planar boards, PV denotes the planar hut surfaces, G denotes ground patches, L denotes light poles, and LH denotes linear hut ridges. Here, the HDL-32E1 and HDL-32E2 scanners are taken as reference and slave units, respectively.

First, all the points are reconstructed using initial estimates of the mounting parameters, which are obtained from manual measurements/estimates for the lever-arm and boresight angles between SPAN-CPT and reference laser unit, and between the reference and slave laser units. Then, the semi-automatic feature extraction is executed to obtain the points for planar features (i.e., high reflective boards, ground patches, and planar patches of huts) and for linear/cylindrical features (i.e., light poles and ridge of huts) from all the datasets separately. Finally, the proposed multi-LiDAR unit calibration procedure is applied to obtain the mounting parameters for both the sensors simultaneously, using point pairs from conjugate features in the HDL-32E1 and HDL-32E2 datasets. The accuracy of

TABLE 5.1
Mounting parameters of HDL-32E1 and HDL-32E2 before and after multi-sensor calibration

	ΔX (m)	ΔY (m)	ΔZ (m)	$\Delta\omega$ (deg)	$\Delta\varphi$ (deg)	$\Delta\kappa$ (deg)
	HDL-32E1 LiDAR Unit Mounting Parameters ($r^b_{HDL32E1}$)($R^b_{HDL32E1}$)					
Initial	0.45	0.2	0.32	-5	0	-50
Final	0.487	0.219	0.32	-5.898	0.645	-53.498
Standard Deviation	0.0064	0.0063	0	0.0095	0.0100	0.0134
	HDL-32E2 LiDAR Unit Mounting Parameters ($r^{HDL32E1}_{HDL32E2}$) ($R^{HDL32E1}_{HDL32E2}$)					
Initial	-0.289	-0.344	0	0	0	-15
Final	-0.281	-0.414	-0.005	-0.802	-0.109	-12.541
Standard Deviation	0.0056	0.0054	0.0039	0.0094	0.0104	0.0126

TABLE 5.2
Correlation matrix of mounting parameter estimates from multi-sensor calibration

	ΔX_1	ΔY_1	ΔZ_1	$\Delta\omega_1$	$\Delta\varphi_1$	$\Delta\kappa_1$	ΔX_2	ΔY_2	ΔZ_2	$\Delta\omega_2$	$\Delta\varphi_2$	$\Delta\kappa_2$
ΔX_1	1.000	0.061	0.000	0.021	0.099	0.146	0.163	0.120	0.059	0.007	0.073	0.274
ΔY_1	0.061	1.000	0.000	0.003	0.119	0.309	0.016	0.097	0.286	0.005	0.016	0.058
ΔZ_1	0.000	0.000	0.000	0.000	0.000	0.000	0.000	0.000	0.000	0.000	0.000	0.000
$\Delta\omega_1$	0.021	0.003	0.000	1.000	0.047	0.008	0.038	0.015	0.217	0.364	0.019	0.008
$\Delta\varphi_1$	0.099	0.119	0.000	0.047	1.000	0.304	0.018	0.000	0.242	0.067	0.001	0.025
$\Delta\kappa_1$	0.146	0.309	0.000	0.008	0.304	1.000	0.046	0.038	0.079	0.001	0.010	0.046
ΔX_2	0.163	0.016	0.000	0.038	0.018	0.046	1.000	0.056	0.060	0.058	0.014	0.067
ΔY_2	0.120	0.097	0.000	0.015	0.000	0.038	0.056	1.000	0.134	0.030	0.121	0.402
ΔZ_2	0.059	0.286	0.000	0.217	0.242	0.079	0.060	0.134	1.000	0.171	0.389	0.071
$\Delta\omega_2$	0.007	0.005	0.000	0.364	0.067	0.001	0.058	0.030	0.171	1.000	0.040	0.017
$\Delta\varphi_2$	0.073	0.016	0.000	0.019	0.001	0.010	0.014	0.121	0.389	0.040	1.000	0.196
$\Delta\kappa_2$	0.274	0.058	0.000	0.008	0.025	0.046	0.067	0.402	0.071	0.017	0.196	1.000

calibration procedure is evaluated by monitoring the a-posteriori variance factor after every iteration of the least squares adjustment (LSA) procedure and also, the RMSE of the normal distance of points belonging to a planar or linear/cylindrical feature from its best-fitting plane or line, respectively.

The initial approximations of these mounting parameters and the final results (along with their standard deviations) from the multi-sensor calibration for HDL-32E1 as well as HDL-32E2 sensors are listed in Table 5.1. One should note that the lever arm ΔZ for the reference sensor (here, HDL-32E1) is fixed during the calibration procedure, which is marked in red color in Table 5.1. The correlation matrix for the estimated mounting parameters of the two sensors is also listed in Table 5.2, which indicates that none of the parameters are highly correlated. The average normal distance between conjugate features in overlapping drive runs after calibration can be quantified by the square root of the a-posteriori variance factor ($\hat{\sigma}_o$), which is 1.72 cm in this case. This is better than the expected accuracy of around 3 cm according to the LiDAR Error Propagation Calculator. Furthermore, through the qualitative evaluation depicted in Figure 5.8, one can observe a significant improvement of boards, ground patches, and light poles after calibration. The $\hat{\sigma}_o$ value of the LSA procedure and the RMSE of normal distance of

points from best-fitting plane/line for extracted features after every iteration are listed in Table 5.3.

It can be seen from Table 5.3 that the RMSE for each feature is consistently improving after every iteration. The final RMSE for all the calibration primitives can be seen to be about 1–4 cm. One should note that the designed boards have a thickness of about 1 cm, so their RMSE can never be less than a centimeter. These qualitative and quantitative results indicate that the proposed calibration strategy is efficient and accurate.

5.2.2 Quantitative Evaluation from Highway Dataset

A highway dataset captured on 2017/09/19 with drive-runs aligned in different directions (i.e., south-bound and north-bound) is used to check the alignment between the point clouds obtained from different sensors and drive-runs. From the highway dataset, a bridge and the barriers used to channelize devices are extracted to check the alignment, as shown in Figure 5.9. In Figure 5.9 (a), the point clouds from left and right sensors in south-bound drive-run as well as left and right sensors in north-bound drive-run are colored in green, orange, blue, and pink, respectively. From the Figure 5.9 (b), one can note that there is a discrepancy of around 6 cm between the point clouds acquired in south-bound and north-bound drive-runs. However, the point clouds from
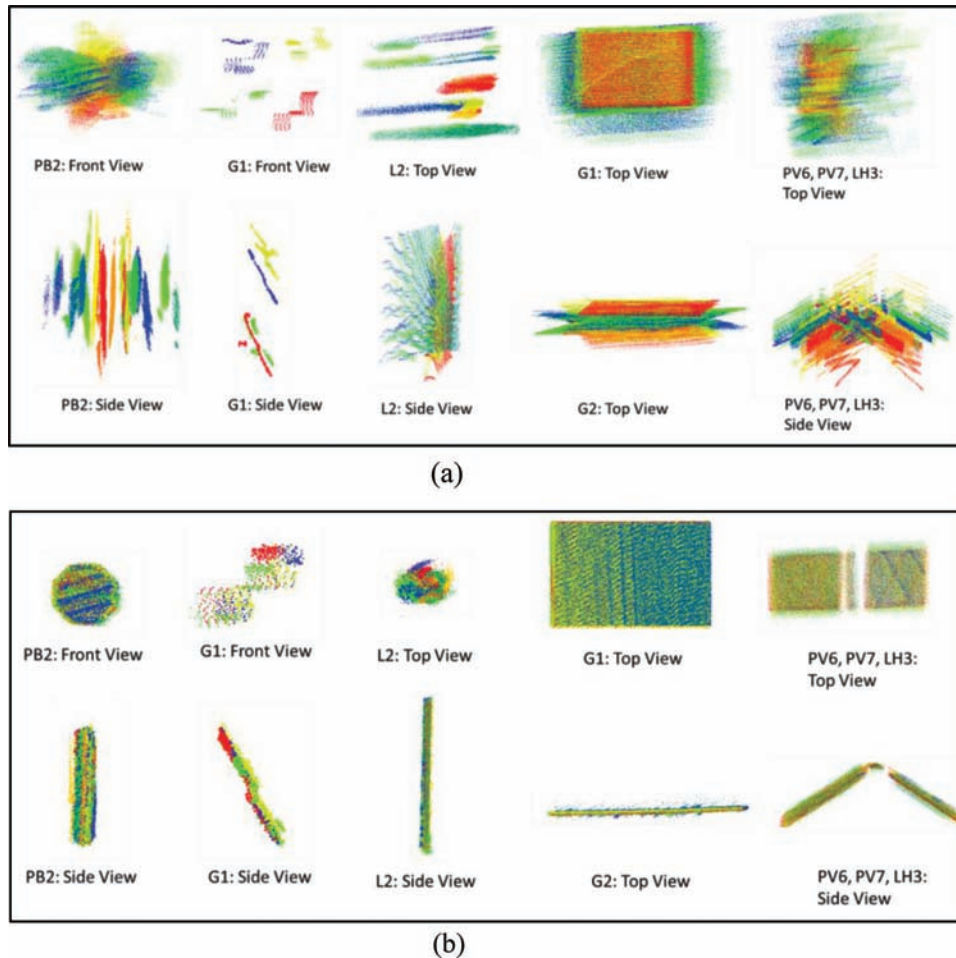
Figure 5.8 Qualitative evaluation of some of the extracted boards, ground patches, and light poles (a) before calibration, and (b) after calibration.

the left and right sensors are aligned well in a single drive-run. One should note that this discrepancy between different drive-runs is not clearly identifiable when we inspect a large scale object (e.g., bridge, as shown in Figure 5.9 (c-d)).

5.2.3 Repetitive Testing of Calibration Procedure

The mobile mapping system was mounted on different cars for every mission. To ensure the accuracy of the acquired point clouds, the calibration procedure was carried out every time before proceeding with acquiring data along a road. There are six datasets used in the next chapter for lane width estimation. Two datasets were collected for an interstate highway; three datasets were collected for a U.S. highway; and one dataset was collected for a main arterial. These six datasets are captured on different dates and using different sensors (i.e., HDL-32E or VLP-16). The mounting parameters derived from the introduced multi-unit LiDAR system calibration procedure for each of the six datasets are listed in Table 5.4.

TABLE 5.3
HDL-32E1 + HDL-32E2 multi-sensor calibration: A-posteriori variance factor ($\hat{\sigma}_o$) and RMSE of plane/line fitting

|	Number of LiDAR Points	Before Calibration	Calibration Iteration 1	Calibration Iteration 2	Calibration Iteration 3
$\hat{\sigma}_o$ (m)			0.0394	0.0172	0.0172
			RMSE (m)		
Feature ID			**Reflective Boards**		
Board 0	20,240	0.304	0.018	0.020	0.020
Board 1	78,063	0.333	0.025	0.028	0.028
Board 2	105,320	0.252	0.026	0.028	0.028
Board 3	47,323	0.335	0.028	0.030	0.030
Board 4	1,022	0.112	0.010	0.013	0.013
Board 5	664	0.120	0.012	0.016	0.016
Board 6	4,466	0.157	0.019	0.020	0.020
Board 7	10,464	0.164	0.015	0.017	0.017
			Ground Patches		
Ground 0	802,878	0.164	0.016	0.016	0.016
Ground 1	956,653	0.172	0.015	0.014	0.014
Ground 2	988,163	0.155	0.017	0.016	0.016
Ground 3	1,209,071	0.175	0.016	0.016	0.016
			Hut Surfaces		
Surface 0	67,644	0.253	0.029	0.030	0.030
Surface 1	40,461	0.270	0.036	0.038	0.038
Surface 2	69,739	0.243	0.023	0.023	0.023
Surface 3	89,144	0.288	0.031	0.031	0.031
Surface 4	77,916	0.233	0.031	0.032	0.032
Surface 5	97,395	0.228	0.034	0.037	0.037
Surface 6	77,329	0.275	0.030	0.031	0.031
Surface 7	50,113	0.238	0.023	0.024	0.024
			Hut Ridges		
Ridge 0	3,775	0.162	0.028	0.020	0.020
Ridge 1	5,308	0.184	0.019	0.018	0.018
Ridge 2	7,660	0.190	0.017	0.018	0.018
Ridge 3	4,498	0.166	0.017	0.017	0.017
			Flag Poles		
Pole 0	41,810	0.267	0.028	0.032	0.032
Pole 1	33,929	0.257	0.029	0.033	0.033
Pole 2	39,361	0.254	0.027	0.031	0.031
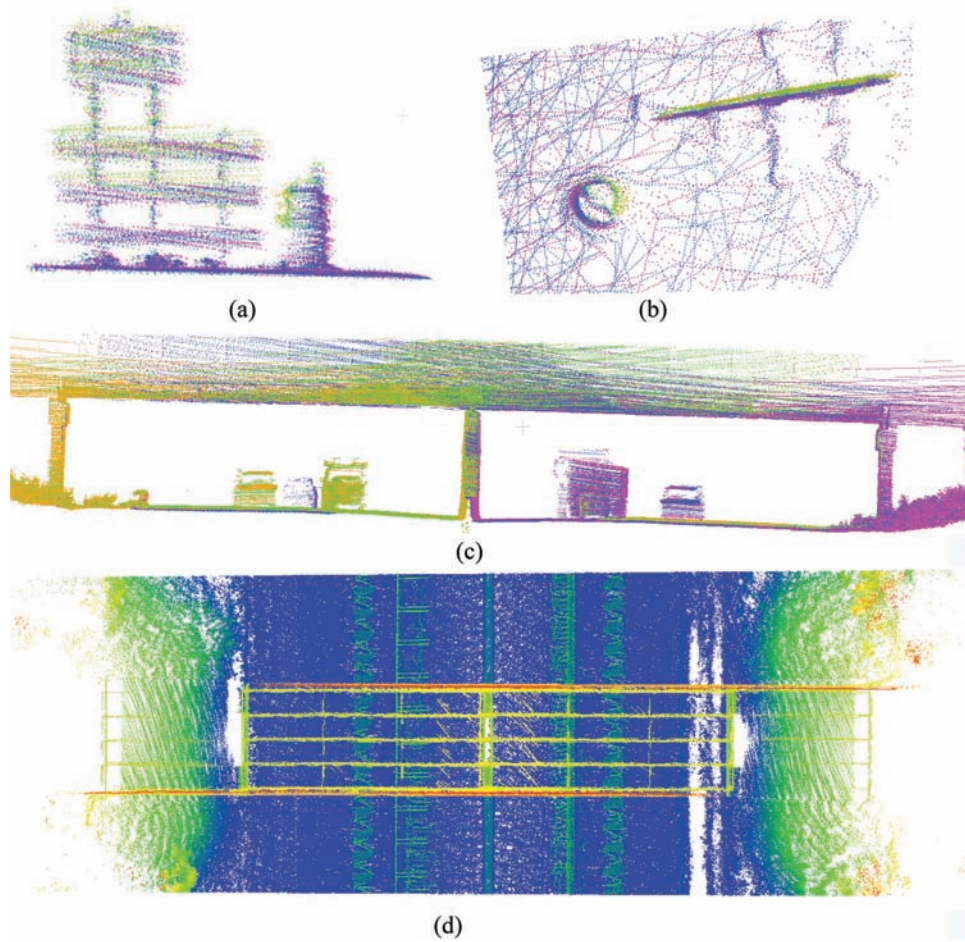
Figure 5.9 Highway objects, (a) front view of barriers channelizing devices colored by different sensors and drive-runs, (b) top view of barriers channelizing devices colored by different sensors and drive-runs, (c) front view of bridge colored by different sensors and drive-runs, and (d) top view of bridge colored by high.

TABLE 5.4
Mounting parameters for the datasets from the multi-unit LiDAR system calibration procedure

Date	Mounting Parameters					
	ΔX (m)	ΔY (m)	ΔZ (m)	$\Delta\omega$ (°)	$\Delta\varphi$ (°)	$\Delta\kappa$ (°)
	Interstate Highway					
2016/11/05	HDL32E-2 Calibration Parameters $R^b_{HDL32E2} r^b_{HDL32E2}$					
	0.471	0.2057	0.3000	-5.868	-0.1548	-54.0072
	VLP16-1 Calibration Parameters $R^{HDL32E2}_{VLP161} r^{HDL32E2}_{VLP161}$					
	-0.271	-0.376	-0.073	-2.092	-4.161	22.014
2017/05/02	HDL32E-2 Calibration Parameters $R^b_{HDL32E2} r^b_{HDL32E2}$					
	0.470	0.196	0.319	-6.110	0.488	-56.728
	HDL32E-3 Calibration Parameters $R^{HDL32E2}_{HDL32E3} r^{HDL32E2}_{HDL32E3}$					
	-0.246	-0.384	-0.003	-0.734	0.1054	-111.320
	U.S. Highway					
2016/11/30	HDL32E-2 Calibration Parameters $R^b_{HDL32E2} r^b_{HDL32E2}$					
	0.476	0.201	0.300	-6.047	-0.095	-58.870
	VLP16-1 Calibration Parameters $R^{HDL32E2}_{VLP161} r^{HDL32E2}_{VLP161}$					
	-0.246	-0.400	-0.089	-1.581	-4.274	26.810
2017/02/11	HDL32E-2 Calibration Parameters $R^b_{HDL32E2} r^b_{HDL32E2}$					
	0.466	0.178	0.324	-6.049	0.456	-63.961
	HDL32E-3 Calibration Parameters $R^{HDL32E2}_{HDL32E3} r^{HDL32E2}_{HDL32E3}$					
	-0.218	-0.378	-0.004	-1.464	-4.425	-105.495
2017/08/17	HDL32E-4 Calibration Parameters $R^b_{HDL32E2} r^b_{HDL32E2}$					
	0.446	0.204	0.322	-5.692	0.941	-53.531
	HDL32E-5 Calibration Parameters $R^{HDL32E4}_{HDL32E5} r^{HDL32E4}_{HDL32E5}$					
	-0.286	-0.375	-0.009	-0.696	-0.478	-12.616
	Main Arterial					
2016/10/11	HDL32E-2 Calibration Parameters $R^b_{HDL32E2} r^b_{HDL32E2}$					
	0.425	0.191	0.300	-5.839	-1.460	-47.953
	VLP16-1 Calibration Parameters $R^{HDL32E2}_{VLP161} r^{HDL32E2}_{VLP161}$					
	-0.298	-0.336	-0.009	-3.537	-3.147	15.996

Note: HDL32E-2, HDL32E-3, HDL32E-4, and HDL32E-5 denote different LiDAR sensors of the same model.

6. LANE WIDTH ESTIMATION STRATEGY

6.1 Methodology of Lane Width Estimation

The proposed methodology for lane width estimation proceeds according to three major steps: (1) road surface and lane marking extraction, (2) derivation of lane marking centerline, and (3) lane width estimation. First, the road surface is extracted with the assistance of vehicle trajectory data. Next, lane markings are extracted along the road surface by identifying high-intensity points. Since lane markings have a certain thickness, their centerline is derived for estimating the lane width. The flowchart of the proposed strategy is shown in Figure 6.1. The following subsections introduce the technical details of these steps.

6.1.1 Road Surface and Lane Marking Extraction

The proposed strategy focuses on lane width estimation along the driving lane. In this section, we introduce a strategy to extract the road surface and lane marking on the road surface along the driving lane. The trajectory data records the information of vehicle position and orientation, which is defined by the position and orientation of the IMU body frame of the GNSS/INS navigation system. Therefore, the LiDAR point cloud pertaining to the road surface can be derived with the help of the trajectory data and the IMU height above road surface. First, road surface points are extracted by setting a height threshold (h_{IMU}) and a threshold (d_w) for lateral distance from the vehicle trajectory, as shown in Figure 6.2. The height threshold (h_{IMU}) is the expected normal distance from the IMU body frame to road surface. It can be derived automatically by first, randomly selecting a trajectory data point and searching the LiDAR point (P_i) with the closest (X, Y) coordinates and the least Z-coordinate. Then, a k-nearest neighbor search is applied to P_i for defining a road surface. A plane-fitting is done to estimate the parameters of the road surface. Finally, the height threshold can be derived from the normal distance between the trajectory data point to the fitted plane. Since the road surface may not be flat, a pre-determined buffer for the height threshold (h_{IMU}) is necessary. The height buffer is
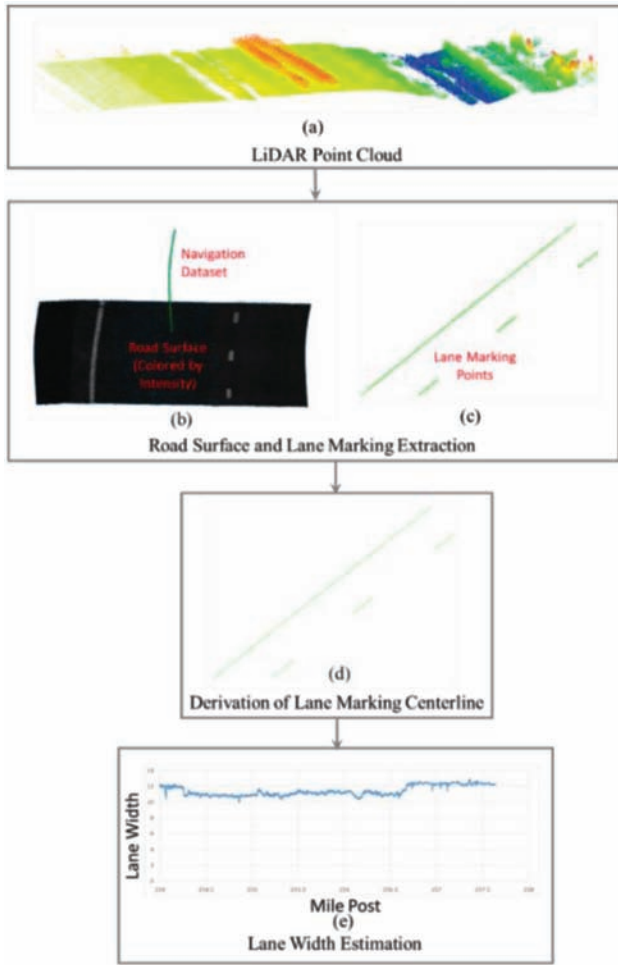
Figure 6.1 Flowchart of the lane width estimation strategy; (a) input LiDAR point cloud (colored by height), (b) extracted road surface, (c) candidate lane marking points, (d) derivation of lane marking centerline, (e) lane width vs. longitudinal distance plot.

illustrated in Figure 6.2. The lateral distance threshold (d_w) is defined for both sides of the trajectory data across its direction and is used to only extract the road surface for the driving lane. When the normal distance between a LiDAR point and the trajectory projection onto the road surface is smaller than d_w as well as its height is within the height buffer, the LiDAR point is regarded as a road surface point, as shown in Figure 6.1 (b). After extracting the road surface, we proceed to extract lane markings. An intensity threshold (Th_I) is pre-defined to extract points representing lane markings. When the intensity of the extracted road surface points is larger than Th_I, they are regarded as potential candidate lane markings, as illustrated in Figure 6.1 (c). One should note that we use a constant pre-defined value for the intensity threshold instead of an adaptive value because the laser beams contributing toward the lane markings along the driving direction would be homogeneously distributed and hence, the intensity value from lane markings will be homogeneous along the entire trajectory.
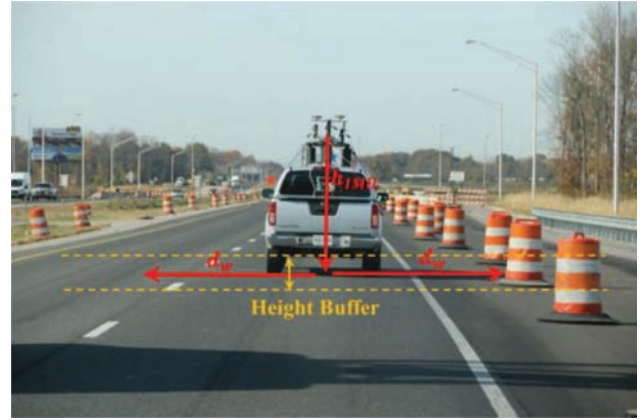

Figure 6.2 Illustration of the various thresholds—height threshold (h_{IMU}) and lateral distance threshold (d_w)—for road surface extraction.

6.1.2 Derivation of Lane Marking Centerline

Since lane markings are strips having a finite width, it is imperative to derive their centerline for lane width estimation. The points extracted as potential candidate lane markings in the previous step may also arise from other features, such as road markings, road surface pavement, and rubble within construction work zones. Therefore, these non-lane marking points should be removed before proceeding to centerline derivation. The derivation of centerline for lane marking segments from the extracted high intensity points is achieved using the following steps: (1) clustering potential candidate lane marking points using a distance-based region growing, (2) partitioning such clusters into subgroups, (3) removal of non-lane marking points, and (4) centerline generation and downsampling to derive centerline segments.

First, a distance-based region growing is conducted to group neighboring high intensity points into clusters. When the number of points in a cluster is less than a threshold (Th_{pt}), the cluster is regarded as non-lane marking and removed, as shown in Figure 6.3 (a-b). Since road lanes may not be straight, each cluster is divided into small segments along its main direction (as derived from PCA). These partitioned segments can be assumed to be straight, as illustrated Figure 6.3 (c). Next, non-lane marking points of each segment are detected and removed using a Random Sample Consensus (RANSAC) strategy and trajectory. RANSAC algorithm randomly selects a minimal number of data points required to construct an estimate of a model and then, checks the number of points from the entire dataset that are consistent with the estimated model. Here, the model estimate consists of line parameters. Therefore, two randomly selected points are used to define a straight line. Then, the normal distances of the remaining points within the partitioned segment to the line are calculated. If the normal distance of a point is larger than a threshold (W_{lane}), it would be regarded as an outlier. On the other hand, the points with normal distance lying within the threshold (W_{lane}) are regarded as inliers, thus constituting a consensus set for the

corresponding model. The threshold (W_{lane}) is defined according to the expected width of a lane marking. This procedure is repeated a certain number of times while keeping track of the estimated models and their corresponding consensus set size. The model with the largest consensus set is designated to be the best model. Finally, the largest consensus set is regarded as points belonging to lane marking, as depicted in Figure 6.3 (d), and utilized to derive the centerline parameters of the segment using an LSA model-fitting.

One should note that RANSAC can only remove outliers within a segment but cannot deal with the case where the entire segment does not represent a lane marking. In this case, the trajectory data is utilized to identify segments that do not belong to lane markings. The lane markings are assumed to be always parallel to the vehicle trajectory. Therefore, we can use this characteristic to determine whether a segment represents lane marking or not. When the direction of a segment is similar to the trajectory, it is regarded as a lane marking segment, as shown in Figure 6.3 (e). A segment is represented by the centerline parameters of the segment (a direction vector and a point along the vector). In order to generate a centerline segment, all the points in the consensus set of the segment are projected onto the LSA-based centerline, as illustrated in Figure 6.3 (f). In this case, the projected points would be dense and a down-sampling strategy is applied to reduce the number of the projected points, as depicted in Figure 6.3 (g). When applying the down-sampling strategy, the sample points are picked within a segment at a fixed distance interval, as shown in Figure 6.3 (g).

6.1.3 Lane Width Estimation

The lane width is derived as the normal distance between the centerlines of lane markings located on opposite sides of the trajectory along the driving lane. First, two trajectory data points closest to the queried centerline point are searched to define a trajectory vector along the driving direction. Then, the queried centerline point can be determined to be lying either to the left or to the right side of the trajectory vector. After identifying the left and right lane markings, as shown in Figure 6.4 (a) by the blue dash line and red side line, the normal distance from a point on one side to the straight line defined by the two closest points on the other side can be derived and regarded as lane width, as illustrated in Figure 6.4 (b).

However, the lane markings may not be continuous (e.g., dash line or lane markings without strong reflection). In such cases, they could lead to inaccurate estimation of the normal distance. Hence, an interpolation between the centerline points is applied first to fill the gaps, as shown in Figure 6.4 (c). Figure 6.4 (d) provides an example to show the inaccuracy in the derived normal distance when the interpolation is not applied.
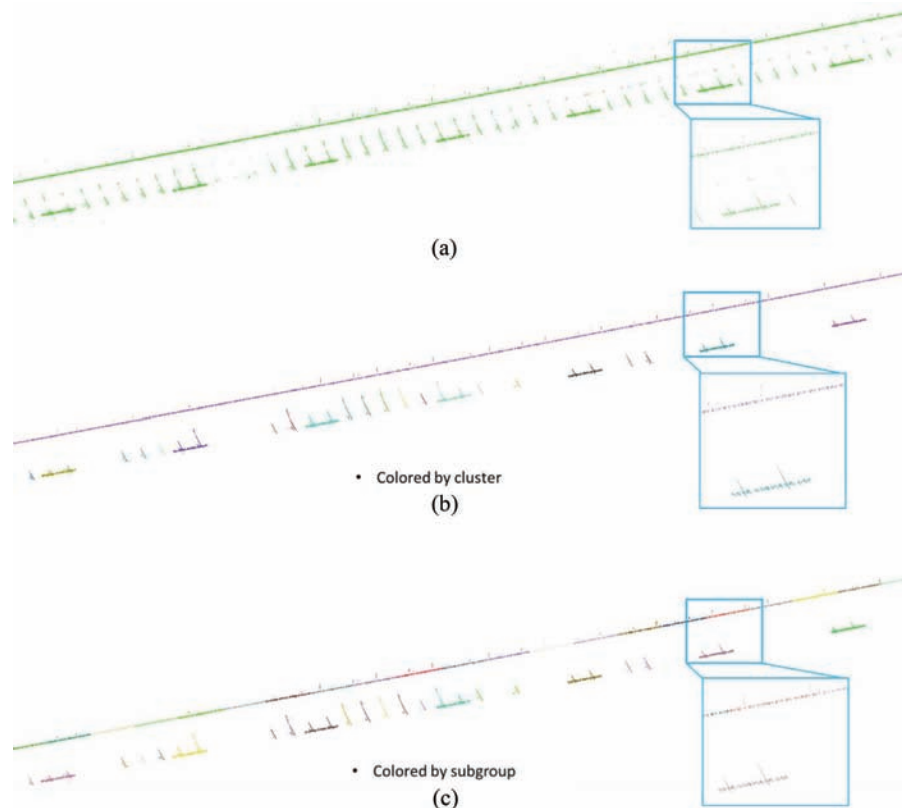
Figure 6.3 Estimation of lane marking centerline (a) candidate lane marking points, (b) region growing-based clustering, (c) cluster partition, (d) outlier removal: RANSAC-based, (e) outlier removal: trajectory-based, (f) lane marking centerline, (g) down-sampled lane marking centreline. (Figure continued next page).

• Colored by subgroup

(d)

• Colored by subgroup

(e)

• Colored by cluster

(f)

• Colored by cluster

(g)

Figure 6.3 (Continued)

Figure 6.4 Lane width estimation procedure; (a) illustration of opposite-side lane marking centerlines, (b) lane width derivation, (c) interpolation among lane marking centerlines, and (d) inaccuracy in lane width estimation without centerline interpolation.

One should note that after the interpolation, the normal distance derived from a point on the left side to the straight line defined by the two closest points on the right side would be similar to the normal distance derived from a point on the right side to the straight line defined by the two closest points on the left side.

6.2 Experimental Results and Analysis

6.2.1 Description of Datasets

To illustrate the performance and feasibility of the proposed calibration strategy and lane width estimation methodology, this section provides experimental results from a total of six datasets collected for three road segments using different 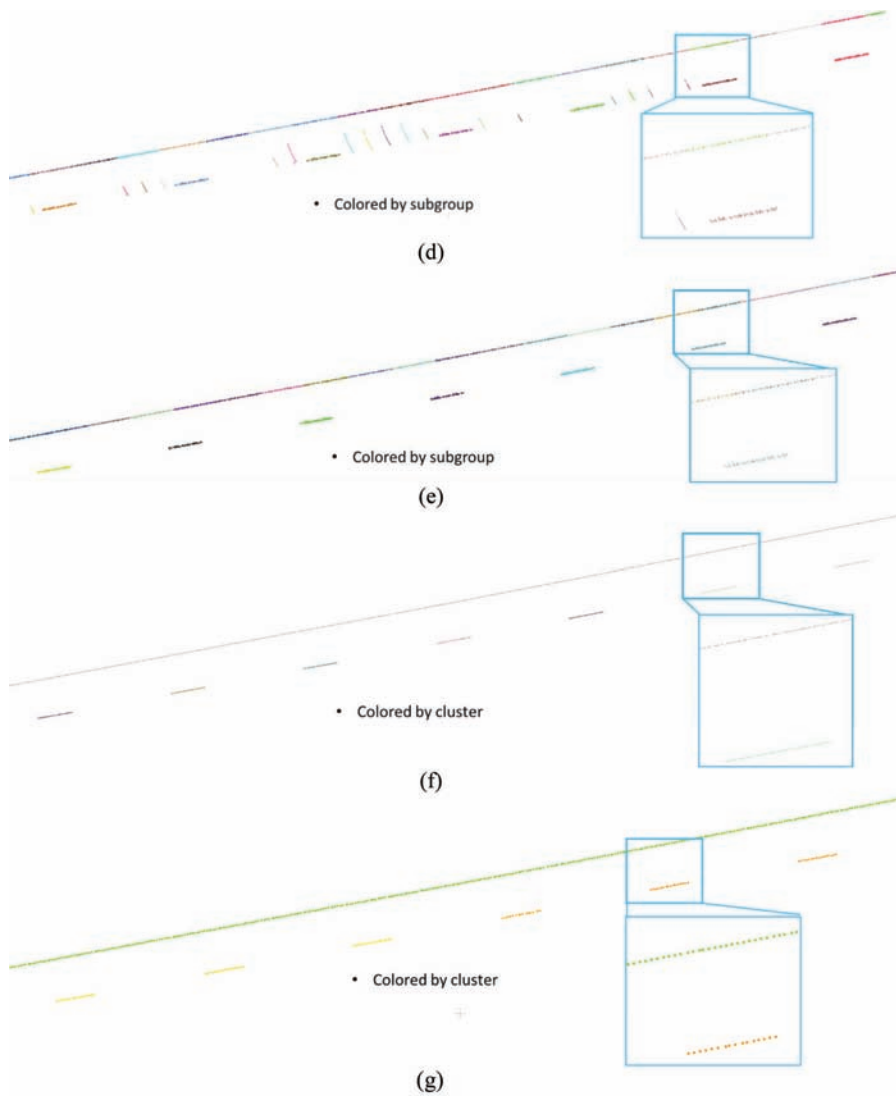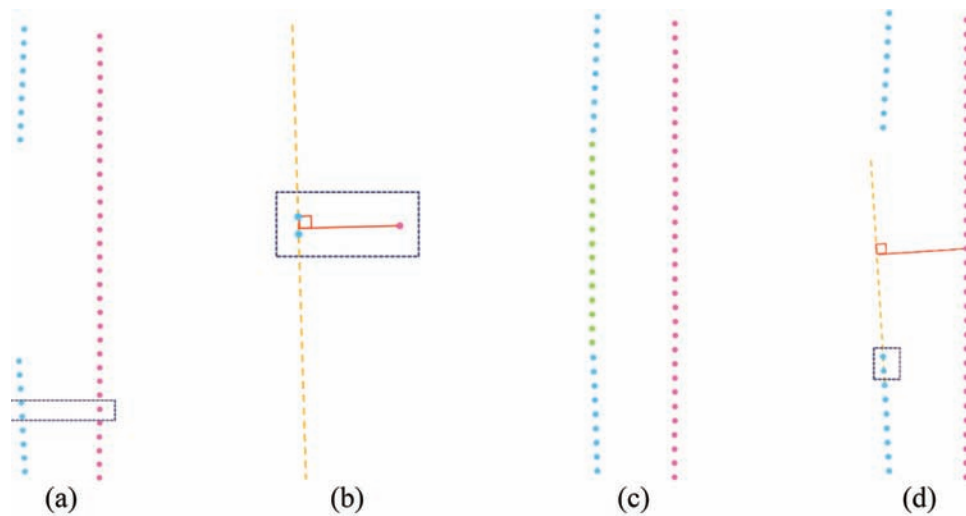sensors in different seasons. A total of four different HDL-32E sensors and one VLP-16 sensor are used to capture these datasets. The first road segment is surveyed on two different days and it is located at an interstate highway work zone area. Both datasets are collected while driving west-bound from mile post 19 to mile post 9 (i.e., a total of 11 miles).

This road segment is highlighted in Google Maps, as shown in Figure 6.5 (a). The second road segment is surveyed on three different days and it is a 3.7 mile long segment located at a U.S. highway, as illustrated in Figure 6.5 (b). The datasets for these two road segments are used for lane width estimation and repeatability analysis of the proposed strategy. The third road segment is located along a main arterial which is a 0.12 mile long segment, as depicted in Figure 6.5 (c). This dataset is used to compare the derived lane width values to on-site manual measurements and lane width from manually digitized lane marking in order to demonstrate the accuracy of the proposed method. The description of the test datasets are listed in Table 6.1.

6.2.2 Experimental Results

In the following four sub-sections, four experiments are discussed. First, we estimated the lane width from a calibrated dataset and then, compared these results to the ones obtained from the same dataset generated after adding a bias to the system mounting parameters.
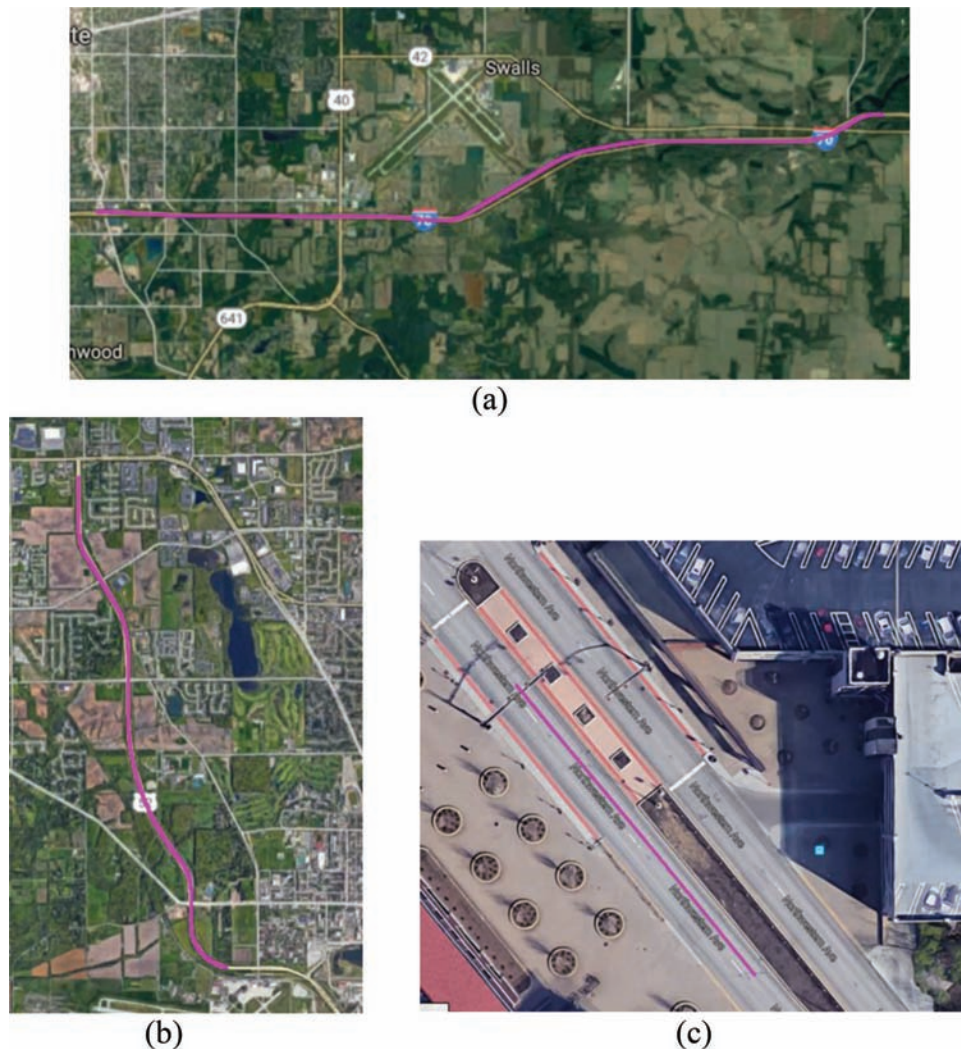

Figure 6.5 Location of test datasets and their trajectory (red), (a) interstate highway, (b) U.S. highway, (c) main arterial.

TABLE 6.1
Description of test datasets collected in this research

Road Segment	Collection Date	Used Sensor	Length	Driving Speed
Interstate Highway	2016/11/05	HDL32E-2 VLP16-1	11 mile	40 mile/hr
	2017/05/02	HDL32E-2 HDL32E-3		40 mile/hr
U.S. Highway	2016/11/30	HDL32E-2 VLP16-1	3.7 mile	40 mile/hr
	2017/02/11	HDL32E-2 HDL32E-3		35 mile/hr
	2017/08/17	HDL32E-4 HDL32E-5		35 mile/hr
Main Arterial	2016/10/11	HDL32E-2 VLP16-1	0.12 mile	20 mile/hr

Note: HDL32E-2, HDL32E-3, HDL32E-4, and HDL32E-5 denote different LiDAR sensors of the same model

TABLE 6.2
Pre-defined thresholds for lane width estimation

Name	Value
Lateral distance threshold for road surface extraction (d_w)	3.0 m
Intensity threshold (Th_I)	30-40
Minimum number of points to define candidate lane marking (Th_{pt})	50 pts
Lane marking width threshold (W_{lane})	0.12 m

This comparison shows the importance of an accurate system calibration to derive accurate lane width estimates. Then, in the second experiment, the 2016/11/30 dataset including two different types of spinning multi-beam laser scanners (i.e., VLP16 and HDL32E) is used to compare their performance in lane width estimation. Moreover, the similarity of derived lane width from the two sensors can demonstrate the accuracy of derived mounting parameters from the introduced multi-sensor system calibration procedure. The third experiment aims to prove the precision of lane width estimation and calibration strategies by comparing the lane width vs mile post plots obtained from five datasets for the interstate highway and U.S. highway (with a total length of approximately 30 miles) scanned by different sensors in different seasons. Finally, the last experiment is conducted to show the accuracy of derived lane width by comparing the results obtained for the dataset collected over the main arterial with that from manually digitized lane marking centerline and on-site manual measurements. The various thresholds used for these experiments are listed in Table 6.2.

6.2.2.1 Impact of Mounting Parameters on Lane Width Estimation.
In this section, point clouds generated from the HDL32E-2 and HDL32E-3 sensors on 2017/02/11 are used to demonstrate that deviations in the mounting parameters would impact the derived lane width estimates. In this experiment, a +2° and -2° bias is added to the boresight parameters ($\Delta\omega$, $\Delta\varphi$, $\Delta\kappa$) of the HDL32E-2 and HDL32E-3 sensors, respectively, to evaluate the effect on lane width estimation from the dataset generated using different estimates of the mounting parameters. One should note that the two cases are characterized only by the difference in mounting parameters and all the other environmental variables, such as sensors, trajectory, time and date of data collection, are identical. Figure 6.6 (a) shows the extracted lane marking points for the dataset generated using accurate as well as inaccurate estimates

of mounting parameters in green and orange colors, respectively. It can be seen that the lane marking points extracted using inaccurate mounting parameters are highly distorted. Figure 6.6 (b-c) shows the derived centerline (in blue) for the two different cases.

The comparison between lane width estimates obtained using the two different sets of mounting parameters is shown in Figure 6.7. The mean, standard deviation, and RMSE values listed in Table 6.3 quantify the effect of inaccurate mounting parameters on the lane width estimation. Table 6.3 shows that compared with the results obtained using accurate estimates of mounting parameters, a change of 2° in the boresight parameters of both sensors results in an RMSE of 27.91 cm. Although the lane width estimation strategy includes outlier removal and LSA-based line fitting that can minimize the effect of inaccurate mounting parameters, it cannot mitigate the effects altogether.

6.2.2.2 Performance Evaluation of Different Sensors.
The lane width estimates derived from point clouds acquired by the VLP16 and HDL32E sensors on 2016/11/30 for the U.S. Highway dataset are used to compare the performance of these units for lane width estimation and to comment on the accuracy of the derived mounting parameters from the introduced multi-sensor calibration procedure. In this experiment, the minimum number of points to define candidate lane marking (Th_{pt}) for the VLP 16 dataset is 25 points, which is half of the one for the HDL32E dataset due to the difference in number of acquired pulses per second. The lane width comparison analysis is shown in Figure 6.8 and the quantitative evaluation is shown in Table 6.4.

The quantitative evaluation in Table 6.4 indicates that the difference between the derived lane width estimates from VLP16 and HDL32E is small, which shows that both sensors are equally capable of accurate lane width estimation. It also implies that the estimated
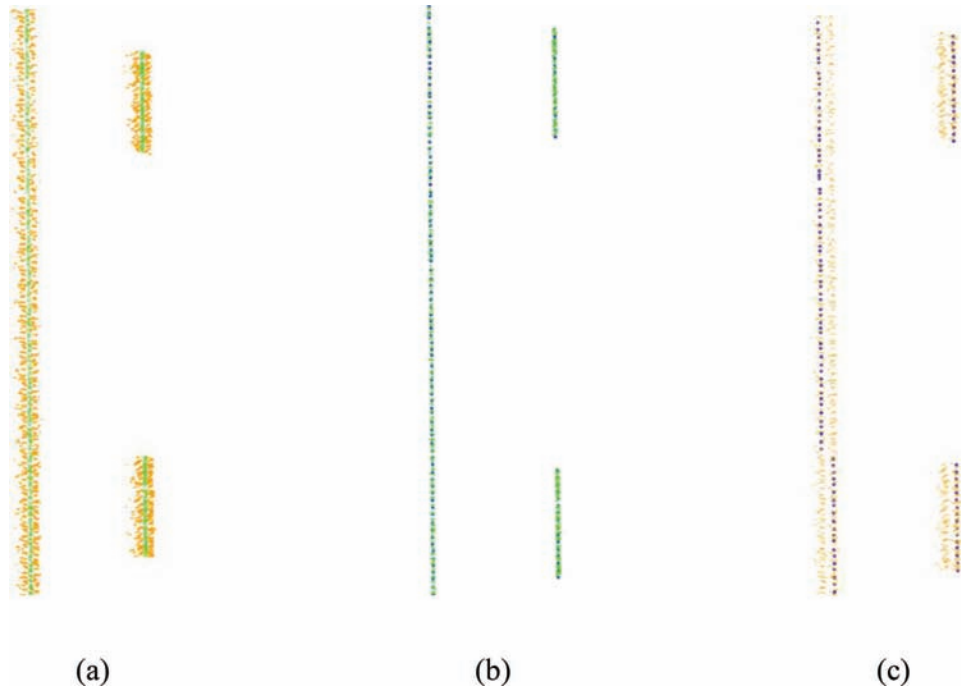
(a)   (b)   (c)

Figure 6.6 Lane marking points and derived centerline, (a) lane marking points (green: using accurate mounting parameters and orange: using inaccurate mounting parameters), (b) lane marking points (green) and derived centerline (blue) using accurate mounting parameters, and (c) lane marking points (orange) and derived centerline (blue) using inaccurate mounting parameters.
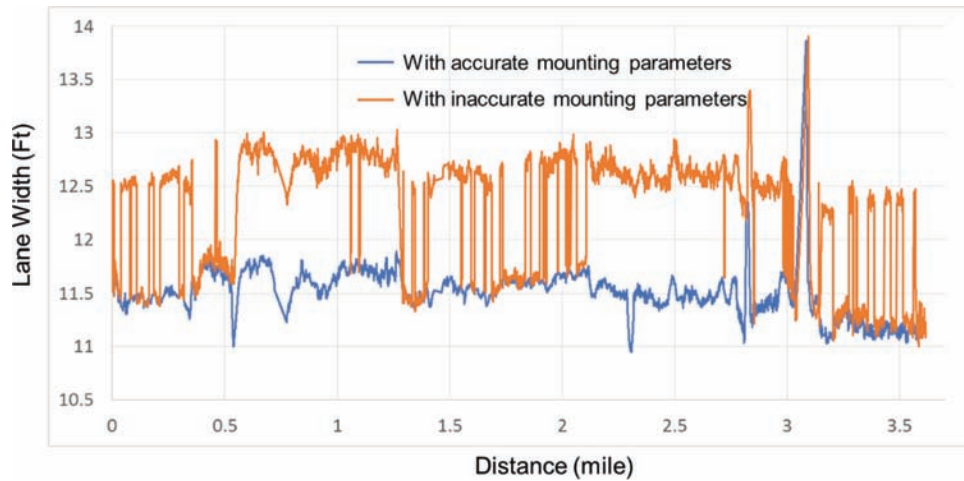
Figure 6.7 Comparison of lane width estimates using accurate and inaccurate values of the mounting parameters for the 2017/02/11 dataset from U.S. highway.

TABLE 6.3
Statistics of comparison between lane width estimates using accurate and inaccurate values of mounting parameters

Compared Datasets	Mean	Standard Deviation	RMSE
2017/02/11 dataset with different estimates of mounting parameters	23.28 cm (0.76 ft)	15.40 cm (0.51 ft)	27.91 cm (0.92 ft)

mounting parameters of the two laser scanners are accurate. However, there is a 0.86ft (26.21 cm) difference in the location highlighted by the green box in Figure 6.8. This difference can be attributed to the sparse nature of the VLP16 point cloud due to which the clustered lane marking points were less than the Th_{pt} threshold so centerline extraction at that location was incomplete and the interpolated centerline could deviate from lane

Figure 6.8 Comparison of estimated lane width from VLP16 and HDL32E for the 2016/11/30 dataset from U.S. highway.
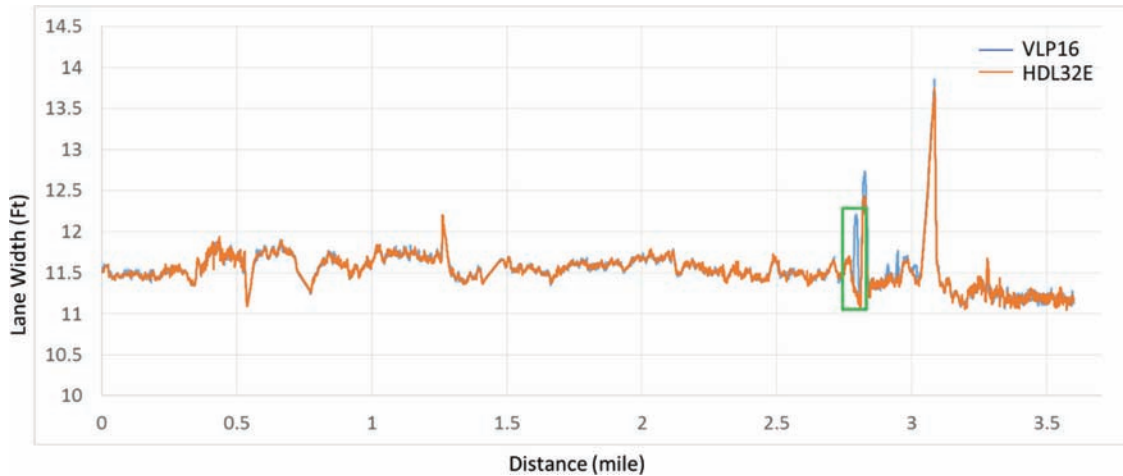
TABLE 6.4
Statistics of lane width comparison of VLP16 and HDL32E

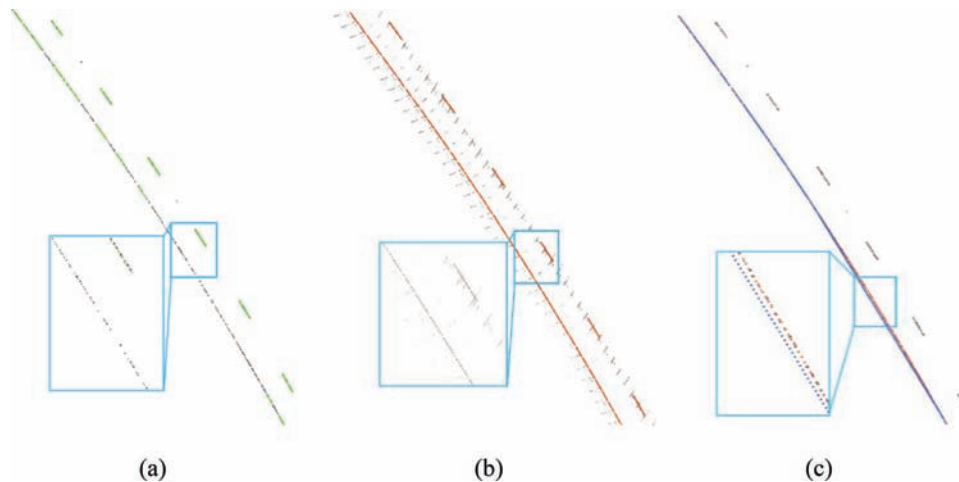| Compared Datasets	Mean	Standard Deviation	RMSE
VLP16 & HDL32E from 2016/11/30	0.007 cm (0.023 ft)	1.53 cm (0.050 ft)	1.68 cm (0.055 ft)

Figure 6.9 Anomalies in the marked area of Figure 6.8, (a) candidate lane marking points (gray) and the derived centerlines (green) from VLP16, (b) candidate lane marking points (gray) and the derived centerlines (red) from HDL32E, and (c) candidate lane marking points from VLP16 (gray), the interpolated centerline from VLP16 (blue), and the derived centerline from HDL32 (red).

markings. This problem was exacerbated by the fact that we have a curved road segment at this location, thus resulting in an inaccuracy in centerline interpolation. Figure 6.9 (a-b) shows the lane marking points (gray) and derived centerline (green and red) from both laser scanners. After interpolation of the derived centerline, as illustrated in Figure 6.9 (c), the maximum deviation in that portion is around 0.86 ft. Since most lane width estimates from VLP16 and HDL32E dataset along this road segment are compatible, the effect of this bias would be insignificant. However, such a discrepancy would not arise in case of a straight portion, as illustrated

in Figure 6.10. This analysis leads us to the conclusion that the lane width estimates from the two sensors are compatible but in order to avoid the discrepancies caused due to the sparse nature of point cloud acquired from VLP16, it is recommended to have slower speed for data collection when using such sensor.

6.2.2.3 Repeatability Analysis of Lane Width Estimation. This section provides an evaluation of the lane width estimation strategy using the datasets collected for two different road segments—an interstate highway segment and a U.S. highway segment. The intensity
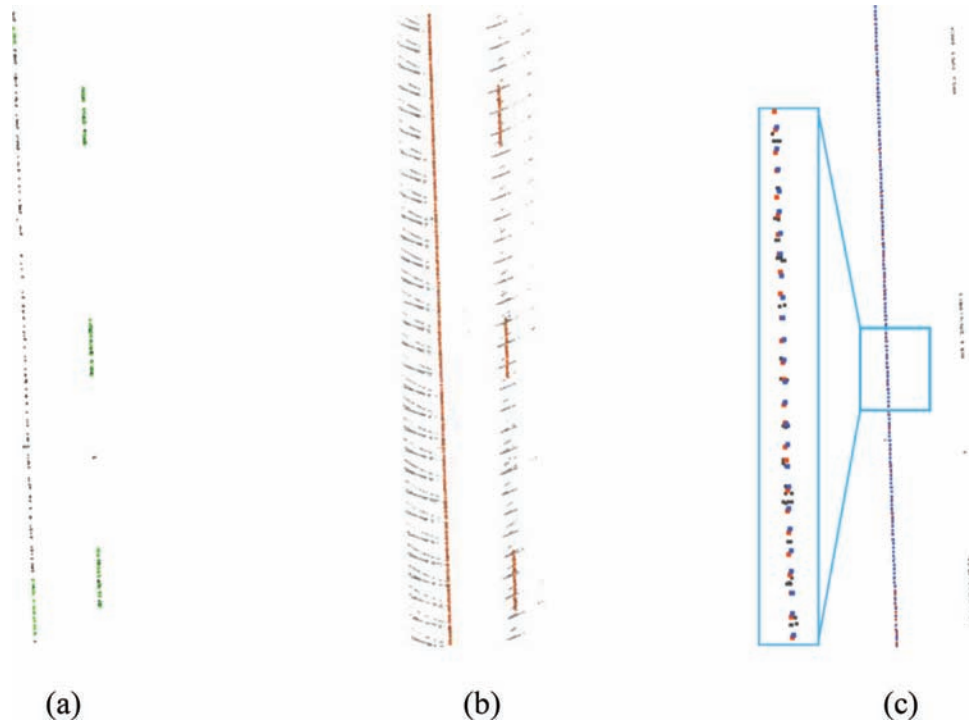
Figure 6.10 Interpolation of straight portion, (a) the derived centerlines (green) and candidate lane marking points (gray) from VLP16, (b) the derived centerlines (red) and candidate lane marking points (gray) from HDL32E, and (c) the interpolated centerline from VLP16 (green), derived centerline from HDL32 (red), and candidate lane marking points from VLP16 (gray).

Figure 6.11 Comparison of estimated lane width from two datasets for the interstate highway section.

for the lane markings could be affected by the used sensor units, weather, incidence angle of laser beams, and quality of lane markings. So, the used Th_I threshold values in the processing of these six datasets varies from 30 to 40 depending on the above factors for each dataset. For the interstate highway segment, two datasets are used to derive the lane width and the obtained values are compared by plotting the lane width vs mile post, as shown in Figure 6.11. In section B of Figure 6.11, because of construction lane closure, we drove on two different lanes so the derived lane width is different. As a result, we only applied the repeatability analysis from mile post 10 to mile post 19. From Figure 6.11, we can notice a

spike in the 2016/11/05 dataset, which is marked by the red box. This spike is attributed to the poor condition of lane markings, as shown in Figure 6.12 (a), which in turn would result in an erroneous lane marking extraction, as illustrated in Figure 6.12 (b). However, this anomaly does not appear in the 2017/05/02 dataset, as shown in Figure 6.13. Since the poor lane markings faded away after six months, the intensity of LiDAR points at that area was not strong as the one from the 2016/11/05 dataset.

For the U.S. highway segment, the comparisons of lane width estimates from three datasets are shown in Figure 6.14. The quantitative evaluation of the

Figure 6.12 Anomalies in 2016/11/05 dataset (a) RGB image, and (b) derived lane marking centerline (green) and extracted lane marking points (gray).

Figure 6.13 2017/05/02 dataset for the area that had poor lane markings in 2016/11/05 dataset.
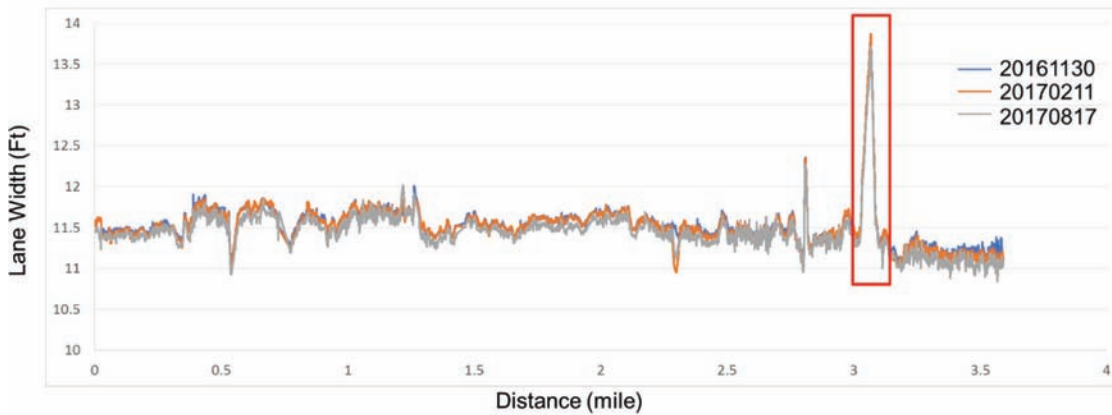
Figure 6.14 Comparison of estimated lane width from three datasets for the U.S. highway segment.

repeatability analysis for the interstate highway and U.S. highway is listed in Table 6.5, which shows that the RMSEs from the comparison results range from 1.49 cm to 3.01 cm, which is acceptable keeping in mind the LiDAR point cloud accuracy obtained from error propagation.

The statistical results demonstrate the repeatability of the proposed strategy when using different sensors to collect data in different seasons and the precision of estimated mounting parameters from the system calibration.

TABLE 6.5
Statistic of lane width comparison from interstate highway datasets and U.S. highway dataset

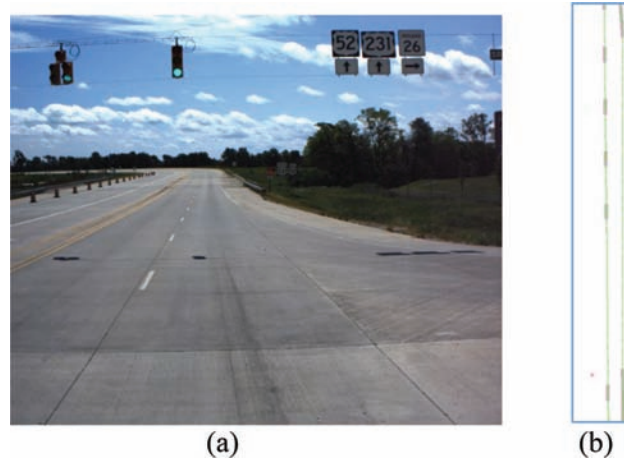| Compared Datasets	Mean	Standard Deviation	RMSE
Interstate Highway			
2016/11/05 & 2017/05/02	1.22 cm (0.040 ft)	1.01 cm (0.036 ft)	1.65 cm (0.054 ft)
U.S. Highway			
2016/11/30 & 2017/02/11	0.85 cm (0.028 ft)	1.22 cm (0.040 ft)	1.49 cm (0.049 ft)
2016/11/30 & 2017/08/17	2.74 cm (0.090 ft)	1.25 cm (0.041 ft)	3.02 cm (0.099 ft)

Figure 6.15 Road intersection area resulting in the spike in Figure 6.14: (a) captured image at the intersection, and (b) extracted lane marking points (pink) and interpolated lane marking centerline (green).

One should note that usually in case of an area corresponding to an intersection, there are no lane markings and hence, the lane width is not defined. Moreover, the lane markings when approaching an intersection area would be curved as they are turning to the other road. Therefore, the interpolated centerlines would be erroneous, thus leading to larger lane width estimates. Figure 6.14 depicts such a case, where the spike within the area marked by the red box is taking place at an intersection and this spike occurs for each of the three datasets. Figure 6.15 (a) shows the corresponding image and Figure 6.15 (b) shows the extracted lane marking points and lane marking centerline after interpolation.

6.2.2.4 Accuracy Analysis of Lane Width Estimation. The main arterial segment is selected for comparing the lane width obtained from the proposed strategy to that from the manually digitized centerline and on-site manual measurements of the corresponding lane width. Figure 6.16 shows the extracted lane markings, their derived centerline as well as the average lane width estimate for each dash line using the proposed strategy. To evaluate the accuracy of the derived lane width, the corresponding value from on-site manual measurements is derived by averaging four values, i.e., distance between inner bounds, outer bounds, inner and outer bounds, and outer and inner bounds of dash line and side lane markings, respectively, as shown in Figure 6.17. Moreover, the lane width derived from a manually digitized centerline is provided to analyze its difference from the lane width estimates obtained from the proposed strategy as well as ground truth. The comparison of the estimated lane width from the proposed strategy and corresponding value from the manually digitized centerline as well as ground truth for each of the three dash lines is shown in Figure 6.18. The difference among derived lane width from the proposed strategy and ground truth is around 0.1 ft (3.04 cm), which validates the accuracy of the lane width estimates from the proposed strategy and also indicates the accuracy of mounting parameter estimates from the system calibration. Also, the difference between the lane width obtained from the manually digitized centerline and ground truth is around 0.04 ft (1.31 cm), which again illustrates the accuracy of mounting parameter estimates.
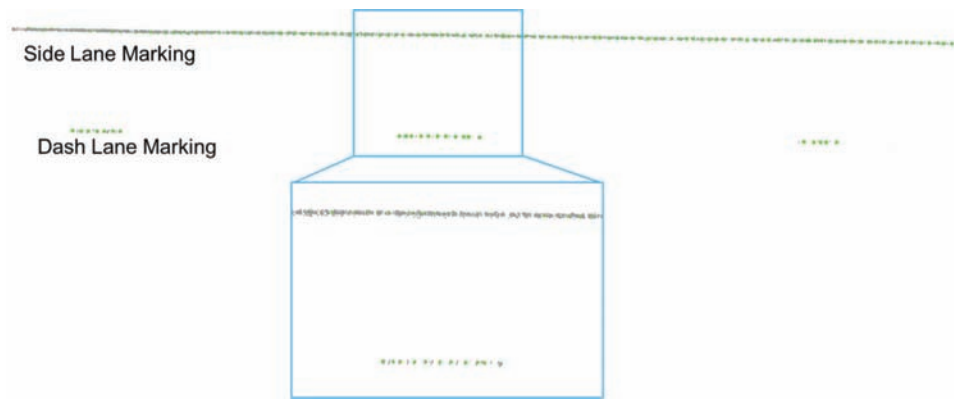
Figure 6.16 Extracted lane marking points (gray) and derived lane marking centerline (green), as well as estimated lane width (unit: ft) using the proposed strategy.
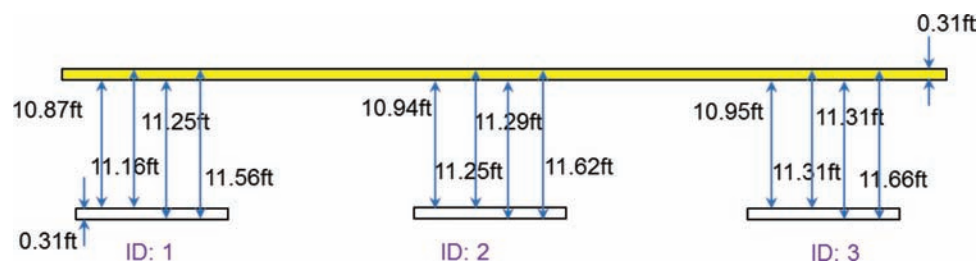

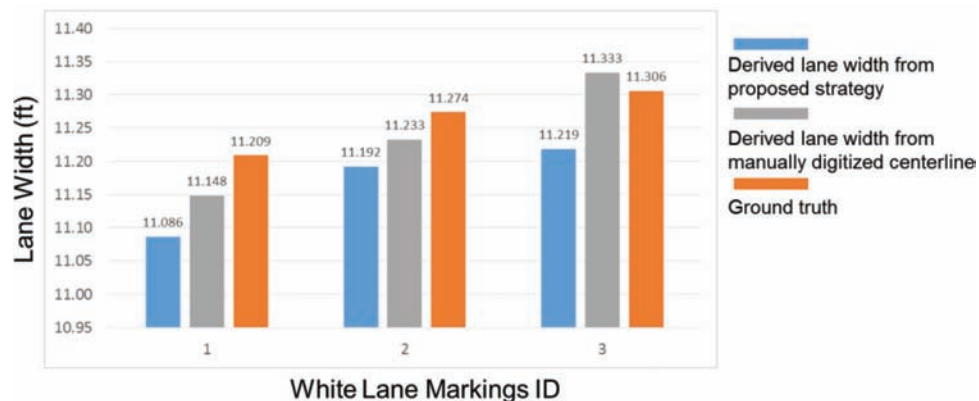**Figure 6.17** On-site manual measurements of lane widths for the main arterial segment.

Figure 6.18 Comparison of derived lane width from proposed strategy and manually digitized centerline as well as ground truth lane width.

7. IMPLEMENTATION

7.1 Data Collection

The first step in the process of data collection is to mount the mapping system onto a mobile platform (here, a car) and test the operation of the different equipment in order to avoid any technical glitches during the course of data collection. The setup of MMS takes about 30 mins and Figure 7.1 shows some images depicting the system setup. As discussed before, each data collection is preceded by a calibration dataset collection for which the calibration targets are set up in an outdoor environment, which is accomplished in another 30 mins, as shown in Figure 7.2. It is followed by 5 mins of dynamic alignment of the GNSS/INS unit and then, a total of approximately 10 mins of drive-runs at an average speed of 4 miles per hour around the calibration test field. After that, work zone data is ready to be collected and needed to be monitored. The driving speed for work zone data collection is around 40 miles per hour. Finally, the data collection is ended with another dynamic alignment of the system for 5 mins.

Figure 7.1   Mounting the mapping system on a car/truck.

Figure 7.2   Deployment of calibration targets.

7.2. Data Processing

7.2.1 3D Point Cloud Reconstruction

The first and foremost step for 3D point cloud reconstruction is the processing of GNSS/INS data to generate the navigation dataset using the post-processing software provided by NovAtel or Applanix (depending on the used GNSS/INS unit), which takes about 30 mins. The Velodyne laser units store the captured data in PCAP format (encoded in a hexadecimal format, as shown in Figure 7.3) that needs to be decoded in order to extract useful information about the scanned points and it is used along with the navigation data and initial estimates of mounting parameters to reconstruct an initial 3D point cloud (in *.las format). The time taken to reconstruct all the PCAP files depends on the amount of data collected and the number of threads used during reconstruction (i.e., the number of PCAP files that are simultaneously reconstructed). For instance, a mission of 2.5 hrs will result in a total of about 82 PCAP files, which would take a total of approximately 1.5 hrs for reconstruction with 5 threads.

7.2.2 System Calibration

After reconstruction, the mounting parameters of MMS are calibrated in order to be able to obtain a point cloud with higher positional accuracy. First, the navigation data is used to extract the beginning and ending times for each of the parallel drive-runs around the calibration targets. Next, the point cloud captured in each drive-run is stored as a separate *.las file. These files are used to carry out a semi-automatic conjugate feature extraction process for calibration by determining seed points for highly reflective sign boards and checkerboards, diagonally opposite corners of ground/wall patches, and end points of linear features. The track separation and feature extraction can be achieved in a total of around 1 hour. Now, the extracted conjugate features are used as input for calibration (which takes about 10 mins), thus resulting in accurate estimates of mounting parameters.
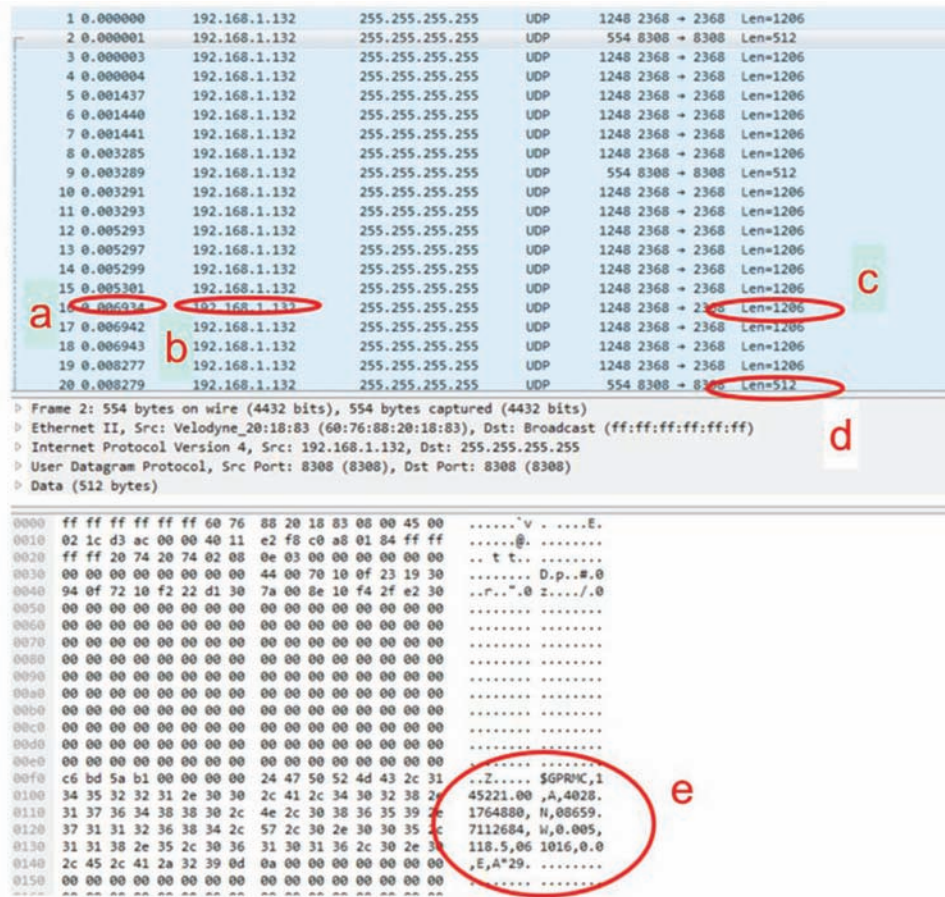
Figure 7.3 Sample PCAP file: (a) time from start of PCAP file, (b) IP address of the LiDAR sensor, (c) length of 1206 bytes corresponds to data packet, (d) length of 512 corresponds to position packet, and (e) GPRMC message encoded within a position packet.

7.2.3 Lane Width Estimation

Having accomplished a successful calibration, all the PCAP files (raw laser scanning measurement) are again reconstructed using the new accurate estimates of mounting parameters to generate revised *.las files (point clouds) that can be used for lane width estimation. In order to estimate lane width, first the road surface is extracted, which takes about 30 mins to 1 hour. Then, the high intensity points representing the lane markings are extracted from the road surface in 5 mins. Then, the navigation data is used along with the high intensity points to derive the lane marking centerline, which requires 10 mins. Finally, the derived centerlines from opposite sides of the road are separated out and then, used to derive the lane width estimates, which takes about 10 mins. Based on these given estimates of time taken for each step, the total data processing time for any collected dataset can be estimated. Table 7.1 summarizes the different tasks involved in the entire process of lane width estimation and their corresponding execution time.

TABLE 7.1
Different tasks involved in lane width estimation and their execution time

Tasks	Execution Time
Data Acquisition	
Mobile mapping system setup	30 mins
Deployment of calibration targets	30 mins
Dynamic alignment (before data collection)	5 mins
Drive-runs around calibration targets	10 mins
Work zone data collection	Variable
Dynamic alignment (after data collection)	5 mins
Data Processing	
3D Point Cloud Reconstruction	
GNSS/INS data processing	30 mins
Initial point cloud reconstruction from PCAP files	Variable
System Calibration	
Track separation and feature extraction	1 hour
Calibration to estimate accurate mounting parameters	10 mins
Lane Width Estimation	
Accurate point cloud reconstruction using new estimates of mounting parameters	Variable
Road Surface Extraction	30-60 mins
Extraction of lane markings	5 mins
Derivation of lane marking centerline	10 mins
Lane width estimation	10 mins

8. CONCLUSIONS AND RECOMMENDATIONS FOR FUTURE WORK

8.1 Conclusions

This report proposed an approach for estimating lane width along the driving lane from dense point clouds acquired by a LiDAR-based MMS. The report started by presenting the system architecture of an MMS comprising several spinning multi-beam laser scanners, camera, and GNSS/INS as well as introducing a LiDAR calibration strategy for deriving the system mounting parameters. In the proposed strategy, the road surface along the driving lane was extracted with the assistance of vehicle trajectory data. Next, lane marking points were extracted based on the assumption that their LiDAR intensity would be higher than those from pavement. A distance-based region growing was applied to cluster potential candidate lane marking points. The clusters were partitioned into subgroups and RANSAC algorithm was used along with the vehicle trajectory information to remove non-lane marking points from the subgroups. Finally, the lane marking centerline was derived from each subgroup for lane width estimation. One should note that a pre-defined threshold is used for extracting the lane marking points. The sensitivity of this threshold depends on the reflectivity of the lane markings. When the reflection from the lane markings is not strong, a lower threshold value is suggested to set up to extract lane markings. In this case, non-lane marking points may also be extracted but the proposed strategy is capable of handling such scenarios and remove the non-lane marking points.

To illustrate the performance of the proposed lane width estimation strategy, we analyzed the results from four different sets of experimental results using a total of six datasets for three different road segments surveyed on different dates using different sensors. The first experiment emphasized the importance of system calibration for deriving accurate lane width estimates by observing the impact of variations in the mounting parameters on lane marking extraction and lane width estimation. The second experiment demonstrated that the VLP16 and HDL32E laser scanners result in compatible estimates for lane width and also, it indicated the accuracy of mounting parameters derived using the proposed multi-sensor calibration strategy. The results from the third experiment proved the repeatability of the proposed lane width estimation strategy by analyzing the precision of the results from multiple datasets for two road segments. Finally, the fourth experiment validated the accuracy of the lane width estimates obtained using the proposed strategy. The precision of the results obtained using the proposed strategy was found to range from 1 cm to 3 cm and the accuracy was around 3 cm, which is acceptable keeping in mind the LiDAR point cloud accuracy obtained from error propagation.

8.2 Recommendations for Future Work

This research only focuses on the driving lane but not neighboring lanes. Future research will be concentrating on deriving lane width from the driving lane as well as neighboring lanes. Currently, there is a requirement to drive in each lane for which lane width needs to be estimated. If the proposed strategy is extended to include lane width estimation for neighboring lanes, it would significantly reduce the time and effort required for dataset collection. LiDAR-based lane width estimation can be expanded by incorporating imagery dataset to
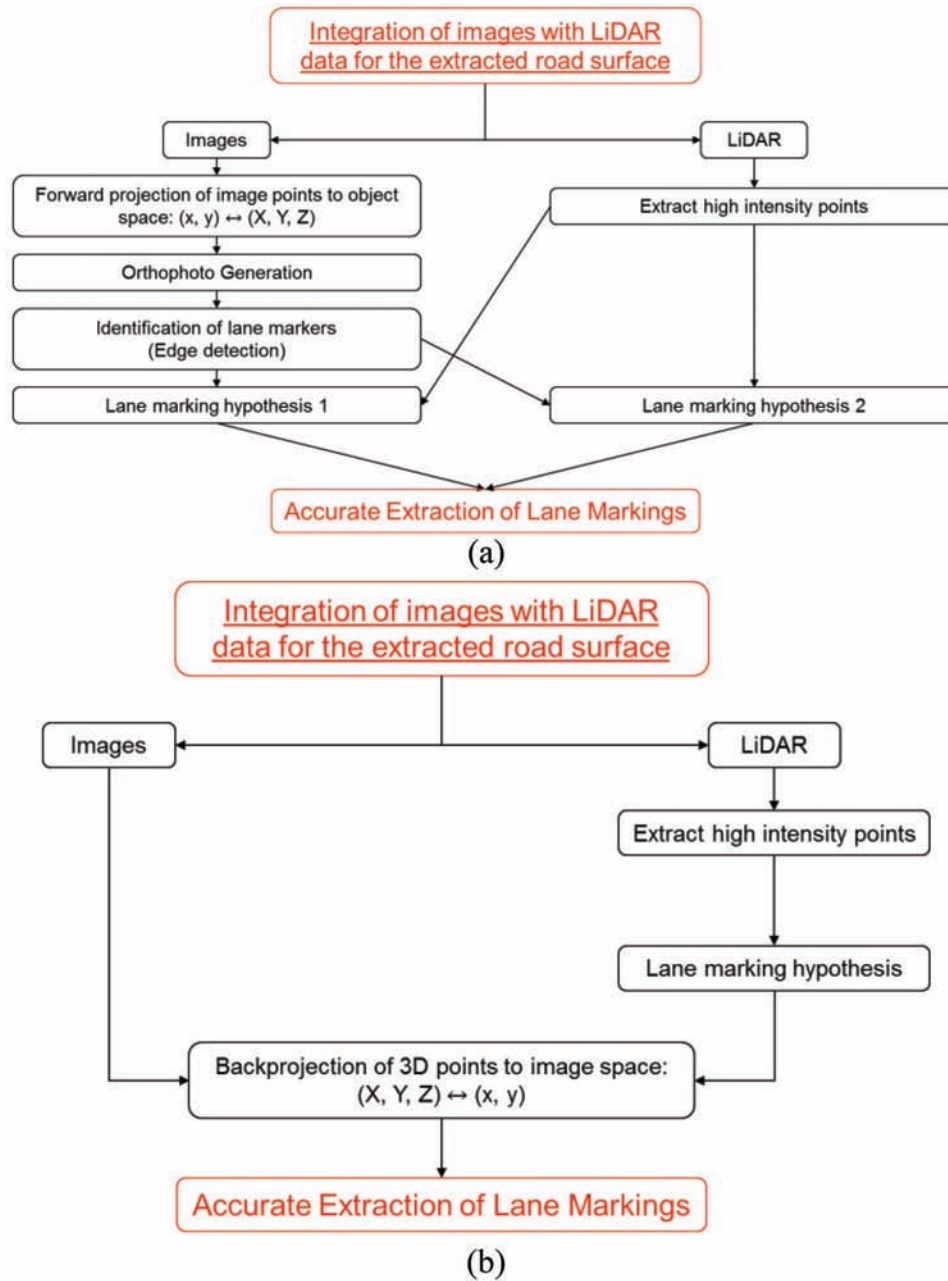
Figure 8.1 Proposed integration of imagery and LiDAR data for lane marking positioning, (a) forward projection strategy, (b) backward projection strategy.

make data analysis more efficient as it would aid in relaxing the sensitivity of the proposed strategy on the intensity value threshold. The flowchart shown in Figure 8.1 depicts a possible strategy for integration of imagery and LiDAR data for positioning of lane markings.

Moreover, after extracting the lane markings, their reflectivity can be analyzed to quantify their visibility. For example, we generated some preliminary results by analyzing the reflection of lane markings from rumble strips having different wavelengths (12, 18, and 24 inches) as well as non-rumble strip area. Image and LiDAR points of lane markings from the rumble strip area

are shown in Figure 8.2. Based on the extracted lane marking points, the cumulative distribution functions from the rumble strip area and non-rumble strip area are shown in Figure 8.3, which indicates that the visibility of lane markings increases with a decrease in the wavelength of rumble strips (i.e., the rumble strips with 12 inch wavelength have higher visibility than those with 18 inch and 24 inch wavelength) and also, the behavior of rumble strips with 12 inch wavelength lane markings is similar to the non-rumble strip lane markings.

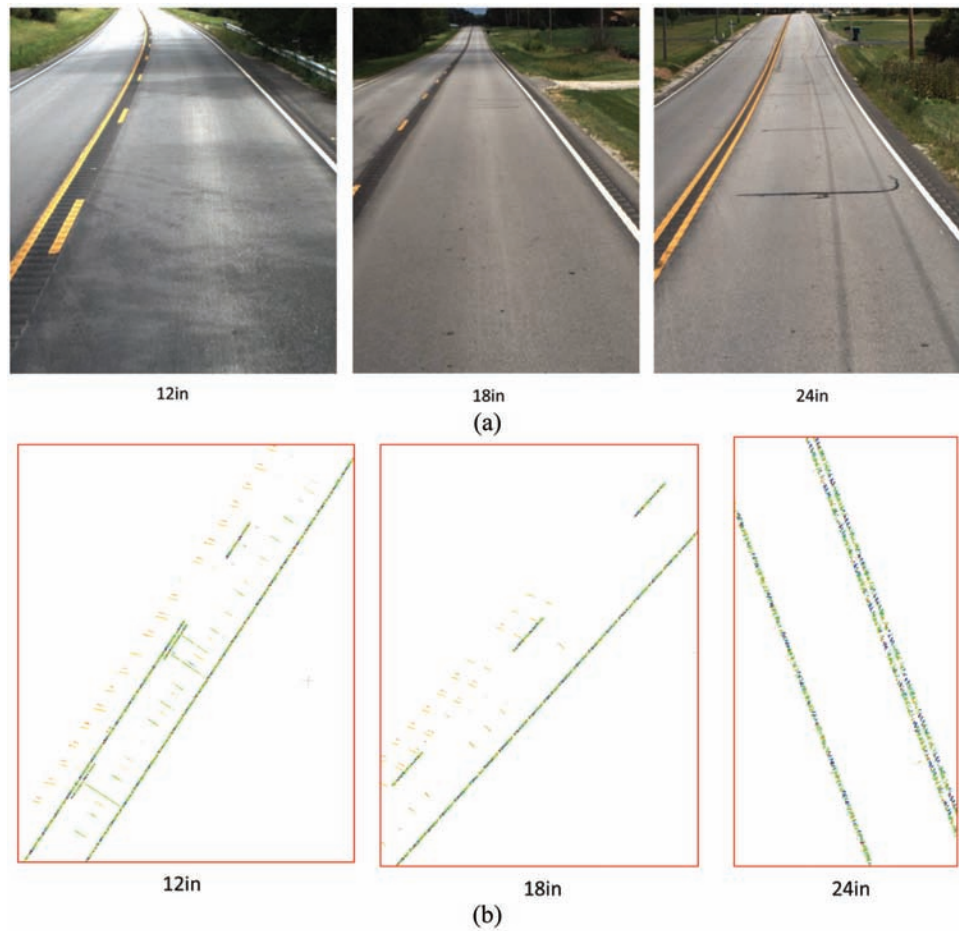Another application where mobile mapping systems can play a vital role is accident scene reconstruction.

Figure 8.2 Rumble strip area with 12 inch, 18 inch, and 24 inch wavelengths: (a) imagery, and (b) lane marking points from two HDL-32E laser scanners.
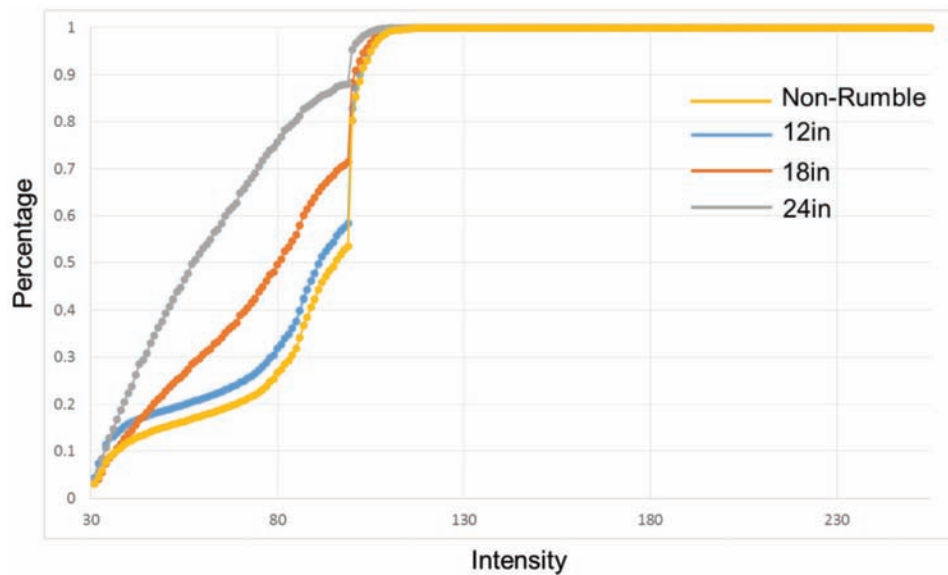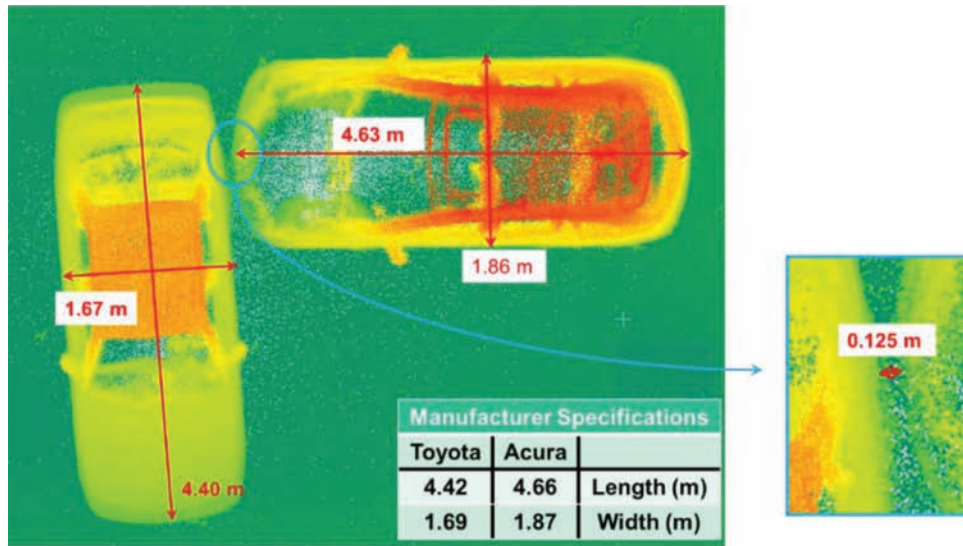

Figure 8.3 Cumulative distribution function for rumble strip and non-rumble strip areas.

(a)

(b)

Figure 8.4 Accident scene reconstruction, (a) LiDAR data colored by height, (b) corresponding imagery for LiDAR data.

The current method used for accident scene reconstruction is time-consuming and could cause congestion due to the lane closure for multiple hours. However, using mobile mapping systems, the data can be collected in an hour and it mitigates the requirement for lane closure. In order to demonstrate such an application, an accident site is simulated and the scene is reconstructed, as shown in Figure 8.4. Additionally, mobile mapping systems can also be used for infrastructure monitoring, such as MSE wall deflection monitoring. Mobile mapping systems have the ability to collect point cloud for several MSE walls in a short time period. The acquired point cloud can be used for deflection monitoring. The preliminary result for MSE wall deflection map is shown in Figure 8.5. The red box in the Figure 8.5 is the investigated

wall. These preliminary results indicate the ability of using LiDAR and photogrammetric data for further analysis in several other aspects of work zone monitoring, transportation applications, and identifying road characteristics.

8.3 Implementation Scenarios

This report has illustrate the capabilities of a LiDAR-based mobile mapping system in precisely and accurately evaluating lane width in work zones while driving at a speed of roughly 40 miles per hour. Operating such a system would require a pre-mission calibration process to derive the mounting parameters relating the LiDAR units to the onboard GNSS/IMU. The implementation
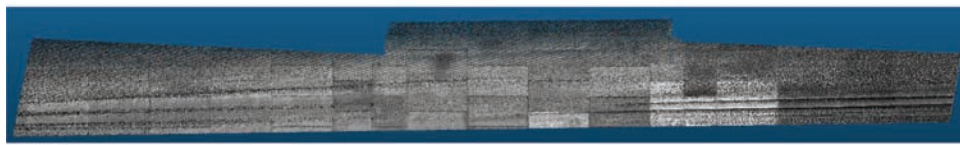
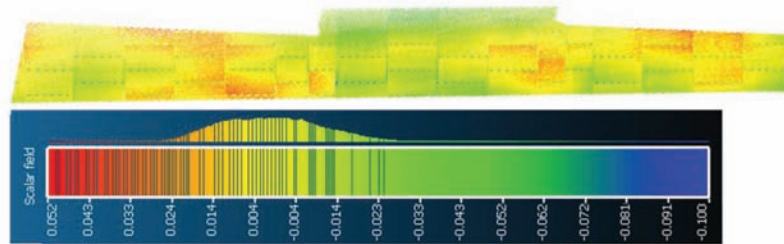**Figure 8.5** MSE wall monitoring, (a) captured imagery from the mobile mapping system, (b) LiDAR data colored by intensity, (c) deflection map (unit: m).

of such a system can be established through one of the following routes:

1. Having a dedicated system at the disposal of INDOT for the collection, processing, and reporting of lane width in work zones in addition to mapping of other features such as signage and tapers. The system could be also used to compare the work zone layout to the Maintenance of Traffic (MoT) design plans.
2. Another alternative would be drafting a set of standard operation and reporting procedures and contracting a Mobile Mapping Surveying outfit to carry the process. For this process, a well-defined Quality Control (QC) measures should be established to quantify the accuracy of the reported lane width estimates.

In either of the above options, a clear reporting mechanism should be established to ensure transparent communication between INDOT and the Project Engineer for the construction work zone to facilitate expedited mitigation of any issues that could affect the traffic flow capacity. One should also keep in mind that this system not only can be used for deriving lane width information but also for reporting the alignment condition of barriers, shoulder width, and taper length. Furthermore, this system can be used to evaluate the reflection of lane markings (which will be a critical factor for Connected and Autonomous Vehicles). Finally, the potential use of such system for accident scene documentation and reduction of accident site clearance should be investigated.

REFERENCES

Atanacio-Jiménez, G., González-Barbosa, J. J., Hurtado-Ramos, J. B., Ornelas-Rodríguez, F. J., Jiménez-Hernández, H., García-Ramirez, T., & González-Barbosa, R. (2011). LiDAR Velodyne HDL-64E calibration using pattern planes. *International Journal of Advanced Robotic Systems*, *8*(5), 70–82. https://doi.org/10.5772%2F50900

Cai, H., & Rasdorf, W. (2008). Modeling road centerlines and predicting lengths in 3-D using LiDAR point cloud and planimetric road centerline data. *Computer-Aided Civil and*

Infrastructure Engineering, 23(3), 157–173. https://doi.org/10.1111/j.1467-8667.2008.00518.x

Chan, T., Lichti, D. D., & Belton, D. (2013). Temporal analysis and automatic calibration of the Velodyne HDL-32E LiDAR system. In M. Scaioni, R. C. Lindenbergh, S. Oude Elberink, D. Schneider, & F. Pirotti (Eds.), *ISPRS annals of the photogrammetry, remote sensing and spatial information sciences* (Vol. II-5/W2, pp. 61–66). Göttingen, Germany: Copernicus Publications. https://doi.org/10.5194/isprsannals-II-5-W2-61-2013

Choi, J. (2014). Hybrid map-based SLAM using a Velodyne laser scanner. In *17th International IEEE Conference on Intelligent Transportation Systems (ITSC)* (pp. 3082–3087). Piscataway, NJ: Institute of Electrical and Electronics Engineers. https://doi.org/10.1109/ITSC.2014.6958185

FHWA. (n.d.). Work zone facts and statistics. Retrieved October 4, 2017, from https://ops.fhwa.dot.gov/wz/resources/facts_stats/safety.htm

Glennie, C., Brooks, B., Ericksen, T., Hauser, D., Hudnut, K., Foster, J., & Avery, J. (2013). Compact multipurpose mobile laser scanning system—Initial tests and results. *Remote Sensing*, 5(2), 521–538. https://doi.org/10.3390/rs5020521

Glennie, C. L., Kusari, A., & Facchin, A. (2016). Calibration and stability analysis of the VLP-16 laser scanner. In J. Skaloud & I. Colomina (Eds.), *The international archives of photogrammetry, remote sensing and spatial information sciences* (Vol. XL-3/W4, pp. 55–60). Göttingen, Germany: Copernicus Publications. https://doi.org/10.5194/isprs-archives-XL-3-W4-55-2016

Ellum, C., & El-Sheimy, N. (2002). Land-based mobile mapping systems. *Photogrammetric Engineering and Remote Sensing*, 68(1), 13–17.

Guan, H., Li, J., Yu, Y., Wang, C., Chapman, M., & Yang, B. (2014). Using mobile laser scanning data for automated extraction of road markings. *ISPRS Journal of Photogrammetry and Remote Sensing*, 87, 93–107. http://dx.doi.org/10.1016/j.isprsjprs.2013.11.005

Habib, A., Lay, J., & Wong, C. (2006). *Specifications for the quality assurance and quality control of LIDAR systems*. Submitted to the Base Mapping and Geomatic Services of British Columbia.

Habib, A. F., Kersting, A. P., Shaker, A., & Yan, W. Y. (2011). Geometric calibration and radiometric correction of LiDAR data and their impact on the quality of derived products. *Sensors*, 11(9), 9069–9097. https://doi.org/10.3390/s110909069

Han, J., Kim, D., Lee, M., & Sunwoo, M. (2012). Enhanced road boundary and obstacle detection using a downward-looking LIDAR sensor. *IEEE Transactions on Vehicular Technology*, 61(3), 971–985. https://doi.org/10.1109/TVT.2012.2182785

He, M., Zhao, H., Davoine, F., Cui, J., & Zha, H. (2013). Pairwise LIDAR calibration using multi-type 3D geometric features in natural scene. In *2013 IEEE/RSJ International Conference on Intelligent Robots and Systems* (pp. 1828–1835). Piscataway, NJ: Institute of Electrical and Electronics Engineers. https://doi.org/10.1109/IROS.2013.6696597

Holgado-Barco, A., González-Aguilera, D., Arias-Sanchez, P., & Martinez-Sanchez, J. (2015). Semiautomatic extraction of road horizontal alignment from a mobile LiDAR system. *Computer-Aided Civil and Infrastructure Engineering*, 30(3), 217–228. https://doi.org/10.1111/mice.12087

Holgado-Barco, A., Gonzalez-Aguilera, D., Arias-Sanchez, P., & Martinez-Sanchez, J. (2014). An automated approach to vertical road characterisation using mobile LiDAR systems: Longitudinal profiles and cross-sections. *ISPRS Journal of Photogrammetry and Remote Sensing*, 96, 28–37. https://doi.org/10.1016/j.isprsjprs.2014.06.017

Kang, Y., Roh, C., Suh, S. B., & Song, B. (2012). A LiDAR-based decision-making method for road boundary detection using multiple Kalman filters. *IEEE Transactions on Industrial Electronics*, 59(11), 4360–4368. https://doi.org/10.1109/TIE.2012.2185013

Kong, H., Audibert, J.-Y., & Ponce, J. (2010). General road detection from a single image. *IEEE Transactions on Image Processing*, 19(8), 2211–2220. https://doi.org/10.1109/TIP.2010.2045715

Kumar, P., McElhinney, C. P., Lewis, P., & McCarthy, T. (2013). An automated algorithm for extracting road edges from terrestrial mobile LiDAR data. *ISPRS Journal of Photogrammetry and Remote Sensing*, 85, 44–55. https://doi.org/10.1016/j.isprsjprs.2013.08.003

Kumar, P., McElhinney, C. P., Lewis, P., & McCarthy, T. (2014). Automated road markings extraction from mobile laser scanning data. *International Journal of Applied Earth Observation and Geoinformation*, 32, 125–137. https://doi.org/10.1016/j.jag.2014.03.023

Lin, H., Gao, J., Zhou, Y., Lu, G., Ye, M., Zhang, C., Yang, R. (2013). Semantic decomposition and reconstruction of residential scenes from LiDAR data. *ACM Transactions on Graphics (TOG)*, 32(4), Article 66. https://doi.org/10.1145/2461912.2461969

Lipski, C., Scholz, B., Berger, K., Linz, C., Stich, T., & Magnor, M. (2008). A fast and robust approach to lane marking detection and lane tracking. In *2008 IEEE Southwest Symposium on Image Analysis and Interpretation* (pp. 57–60). Piscataway, NJ: Institute of Electrical and Electronics Engineers. https://doi.org/10.1109/SSIAI.2008.4512284

Mekker, M. M., Lin, Y. J., Elbahnasawy, M. K. I., Shamseldin, T. S. A., Li, H., Habib, A. F., & Bullock, D. M. (2018) Applications of LiDAR and connected vehicle data to evaluate the impact of work zone geometry on freeway traffic operations. *Transportation Research Record*. https://doi.org/10.1177%2F0361198118758050

Muhammad, N., & Lacroix, S. (2010). Calibration of a rotating multi-beam Lidar. In *Proceedings of the International Conference on IEEE/RSJ Intelligent Robots and Systems (IROS)* (pp. 5648–5653), October 18–22, Toulouse, France.

Novak, K., & Bossler, J. D. (1995). Development and application of the highway mapping system of Ohio State University. *The Photogrammetric Record*, 15(85), 123–134. https://doi.org/10.1111/0031-868X.00012

NovAtel. (2014). *SPAN-CPT user manual* (Rev 8). Calgary, Canada: NovAtel. Retrieved October 18, 2017, from https://www.novatel.com/assets/Documents/Manuals/om-20000122.pdf

Ozturk, O., Ozbay, K., & Yang, H. (2014). Estimating the impact of work zones on highway safety (Paper No. 14-1873). In *TRB 93rd Annual Meeting compendium of papers* [CD-ROM]. Washington, DC: Transportation Research Board.

Puente, I., González-Jorge, H., Martínez-Sánchez, J., & Arias, P. (2013). Review of mobile mapping and surveying technologies. *Measurement*, 46(7), 2127–2145. https://doi.org/10.1016/j.measurement.2013.03.006

Renaudin, E., Habib, A., & Kersting, A. P. (2011). Featured-based registration of terrestrial laser scans with minimum overlap using photogrammetric data. *Etri Journal*, 33(4), 517–527. https://doi.org/10.4218/etrij.11.1610.0006

Schwarz, B. (2010). LIDAR: Mapping the world in 3D. *Nature Photonics*, 4(7), 429–430. https://doi.org/10.1038/nphoton.2010.148

Schwarz, K. P., & El-Sheimy, N. (2007). Digital Mobile mapping systems—state of the art and future trends. In C. V. Tao & J. Li (Eds.), *Advances in mobile mapping technology* (pp. 3–18). London, UK: CRC Press.

Underwood, J., Hill, A., & Scheding, S. (2007, October). Calibration of range sensor pose on mobile platforms. In 2007 IEEE/RSJ International Conference on Intelligent Robots and Systems (pp. 3866–3871). Piscataway, NJ: Institute of Electrical and Electronics Engineers. https://doi.org/10.1109/IROS.2007.4398971

Vallet, B., Xiao, W., & Brédif, M. (2015). Extracting mobile objects in images using a Velodyne LiDAR point cloud. In U. Stilla & C. Heipke (Eds.), *ISPRS annals of the photogrammetry, remote sensing and spatial information sciences* (Vol. II-3/W4, pp. 247–253). Göttingen, Germany: Copernicus Publications.

Velodyne. (2016a). *User's manual and programming guide: HDL-32E high definition LiDAR sensor*. Retrieved October 18, 2018, from https://velodynelidar.com/docs/manuals/63-9113%20REV%20M%20MANUAL,USERS,HDL32E.pdf

Velodyne. (2016b). *Velodyne VLP-16 user manual*. Retrieved October 18, 2018, from https://velodynelidar.com/docs/manuals/63-9113%20REV%20M%20MANUAL,USERS,HDL32E.pdf

Wang, J., Hu, Z., Chen, Y., & Zhang, Z. (2017). Automatic estimation of road slopes and superelevations using point clouds. *Photogrammetric Engineering & Remote Sensing*, *83*(3), 217–223. https://doi.org/10.14358/PERS.83.3.217

Wang, Y., Teoh, E. K., & Shen, D. (2004). Lane detection and tracking using B-Snake. *Image and Vision Computing*, *22*(4), 269–280. https://doi.org/10.1016/j.imavis.2003.10.003

Weiss, U., & Biber, P. (2011). Plant detection and mapping for agricultural robots using a 3D LIDAR sensor. *Robotics and Autonomous Systems*, *59*(5), 265–273. https://doi.org/10.1016/j.robot.2011.02.011

Williams, K., Olsen, M. J., Roe, G. V., & Glennie, C. (2013). Synthesis of transportation applications of mobile LiDAR. *Remote Sensing*, *5*(9), 4652–4692. https://doi.org/10.3390/rs5094652

Yu, Y., Li, J., Guan, H., Jia, F., & Wang, C. (2015). Learning hierarchical features for automated extraction of road markings from 3-D mobile LiDAR point clouds. *IEEE Journal of Selected Topics in Applied Earth Observations and Remote Sensing*, *8*(2), 709–726. https://doi.org/10.1109/JSTARS.2014.2347276

Zhang, W. (2010). Lidar-based road and road-edge detection. In *2010 IEEE Intelligent Vehicles Symposium* (pp. 845–848). Piscataway, NJ: Institute of Electrical and Electronics Engineers. https://doi.org/10.1109/IVS.2010.5548134

About the Joint Transportation Research Program (JTRP)

On March 11, 1937, the Indiana Legislature passed an act which authorized the Indiana State Highway Commission to cooperate with and assist Purdue University in developing the best methods of improving and maintaining the highways of the state and the respective counties thereof. That collaborative effort was called the Joint Highway Research Project (JHRP). In 1997 the collaborative venture was renamed as the Joint Transportation Research Program (JTRP) to reflect the state and national efforts to integrate the management and operation of various transportation modes.

The first studies of JHRP were concerned with Test Road No. 1—evaluation of the weathering characteristics of stabilized materials. After World War II, the JHRP program grew substantially and was regularly producing technical reports. Over 1,600 technical reports are now available, published as part of the JHRP and subsequently JTRP collaborative venture between Purdue University and what is now the Indiana Department of Transportation.

Free online access to all reports is provided through a unique collaboration between JTRP and Purdue Libraries. These are available at: http://docs.lib.purdue.edu/jtrp

Further information about JTRP and its current research program is available at: http://www.purdue.edu/jtrp

About This Report

An open access version of this publication is available online. This can be most easily located using the Digital Object Identifier (doi) listed below. Pre-2011 publications that include color illustrations are available online in color but are printed only in grayscale.

The recommended citation for this publication is: